

Probing nonlinear structure formation beyond Λ CDM with the LSS bootstrap: a joint power spectrum and bispectrum analysis

Giorgia Biselli,^{1,2} Marco Marinucci,³ Guido D’Amico,^{1,2} and Massimo Pietroni^{1,2}

¹*Dipartimento di Scienze Matematiche, Fisiche e Informatiche,
Università di Parma, Parco Area delle Scienze, I-43124, Parma, Italy*

²*INFN Sezione Milano-Bicocca, Gruppo Collegato di Parma, I-43124, Parma, Italy*

³*Institute for Theoretical Physics, ETH Zurich, 8093 Zurich, Switzerland*

(Dated: May 14, 2026)

We present the first MCMC-derived constraints on the parameters of the Large Scale Structure (LSS) bootstrap, a model-independent framework that captures deviations from Λ CDM using symmetry arguments alone. Focusing on modifications to the linear growth rate and to the quadratic perturbation-theory kernel – quantified by the fractional parameters ε_f and ε_{d_γ} , respectively – we carry out a joint analysis of the one-loop galaxy power spectrum and the tree-level bispectrum multipoles within the EFTofLSS, employing the PyBird code extended to implement the bootstrap parametrization. We apply this analysis pipeline to two datasets: the BOSS DR12 LRG sample and the large-volume “PT Challenge” simulations. For BOSS, combining the power spectrum with the bispectrum monopole yields $\sim 7\%$ constraints on ε_f and $\sim 57\%$ constraints on ε_{d_γ} . For the PT Challenge, whose survey volume is about 100 times larger, we reach $\sim 1\%$ precision on ε_f and $\sim 25\%$ on ε_{d_γ} , including the bispectrum quadrupole in the analysis. Our results underscore the complementary roles of ε_f and ε_{d_γ} in separating changes to the background expansion from those affecting nonlinear structure formation, and they show that the LSS bootstrap offers a competitive, model-agnostic method for probing physics beyond Λ CDM with existing and upcoming galaxy surveys.

Contents

I. Introduction	2
II. The Large Scale Structure Bootstrap	2
III. Datasets and tests	4
A. BOSS analysis	5
B. PT Challenge simulations	5
C. Parameters and priors	5
D. Scale cuts	7
E. Degeneracies	9
IV. Results	11
A. BOSS analysis	11
1. A_s free	11
2. A_s fixed	11
B. PT Challenge simulations	13
V. Conclusion and outlook	14
A. Equations of motion and Perturbation Theory Kernels	14
B. Galaxy Power Spectrum and Bispectrum in redshift space	16
C. Impact of A_s Prior Choice	17
D. Theoretical covariance	18
E. Complete parameter space constraints	20

I. Introduction

Ongoing stage-IV galaxy surveys, including *Euclid* [1] and DESI [2], are delivering an unprecedented volume of high-precision cosmological data on galaxy clustering. Maximizing the information extracted from these observations is crucial for subjecting the Λ CDM paradigm to rigorous tests and for uncovering possible hints of physics beyond it. Theoretically, however, a wide variety of extensions to Λ CDM has been put forward, encompassing modified gravity models and alternative dark energy frameworks. Each of these introduces additional parameters and distinct behaviors at both the background and perturbation levels. At the moment, there is no compelling theoretical argument for privileging any one model over the others. As a result, carrying out data analyses individually for every conceivable extension is computationally expensive and lacks strong theoretical motivation. On the observational side, however, extensions of the standard paradigm have attracted increasing attention following the recent data releases from the DESI collaboration, which indicate a mild tension with the Λ CDM concordance model [3–5]. The official analysis is often presented as a scenario in which dark energy evolves with time, but the result that the equation of state is $w < -1$ conflicts with a single-field interpretation and therefore points to more complicated physics. A discussion of additional possible extensions can be found in [6].

These challenges have motivated the construction of model-independent, symmetry-driven parameterizations, which make it possible to explore a broad range of cosmological models within a single, cohesive framework. This is the core principle of the *Large Scale Structure (LSS) bootstrap*, originally introduced in [7] and later generalized in [8, 9] (see also [10] for earlier related work and [11] for extensions). Instead of assuming a specific Lagrangian or fixed equations of motion, the LSS Bootstrap relies solely on the fundamental symmetries of our Universe – such as the Equivalence Principle and rotational invariance – to constrain the analytic structure of the perturbation theory kernels. In this way, it provides a general framework for analyzing large-scale structure data without being tied to specific cosmological scenarios.

In this work, we explore how effectively galaxy clustering measurements can constrain departures from the standard Λ CDM framework, expressed through a set of bootstrap parameters. A first step in this direction was undertaken in [12] (see also [13]), which provided the initial Fisher-matrix forecasts for these parameters for a Euclid-like survey. Here, we perform a state-of-the-art combined analysis of the one-loop galaxy power spectrum and the tree-level bispectrum, both described within the Effective Field Theory of LSS (EFTofLSS) [14–16]. Our numerical work relies on PyBird [17], a fast Python code that computes redshift-space multipoles of biased tracers, which we extend to incorporate the bootstrap parameterization of the perturbation-theory (PT) kernels. The joint posterior distribution is then explored using Markov Chain Monte Carlo (MCMC) methods.

Several recent studies [18–20] have highlighted the extra constraining power provided by bispectrum multipoles relative to analyses based solely on the power spectrum. For instance, [21] reports roughly 5–15% tighter bounds on cosmological parameters when the bispectrum monopole is incorporated, while [22] demonstrates that including the one-loop monopole together with the tree-level quadrupole of the bispectrum yields an improvement of about 13–30% compared with a power-spectrum-only analysis. These works, formulated within the EFTofLSS, have been successfully confronted with both observational data and numerical simulations, and currently define the state-of-the-art in galaxy clustering studies [23–26]. Nonetheless, they rest on the choice of a particular cosmological model. By contrast, the LSS Bootstrap offers a complementary, model-independent framework that enables an efficient exploration of a wide class of theories beyond Λ CDM.

We apply our pipeline both on observational data from the BOSS survey [27] and on mock galaxy catalogs constructed from the ‘PT Challenge’ simulations [28], which cover substantially larger volumes. In doing so, we can evaluate the range of constraints on new physics that can be derived from present-day data and from the measurements attainable by a futuristic survey.

The paper is organized as follows. In Sec. II, we review the Large-Scale Structure (LSS) Bootstrap and introduce the model-independent parameters used to detect possible departures from the Λ CDM framework. Sec. III describes the datasets employed in the analysis, as well as the validation of the analysis pipeline, robustness tests against scale cuts and an investigation of the main degeneracies affecting the inference. The main results are presented in Sec. IV, and conclusions are summarized in Sec. V.

II. The Large Scale Structure Bootstrap

To establish the formalism for a model-independent study of extensions beyond Λ CDM, we start by briefly reviewing the *Large Scale Structure (LSS) Bootstrap* (see [7–9] for more details). This framework offers a neat and systematic

method to construct perturbative kernels based solely on symmetry arguments, thus ensuring broad applicability across a wide range of cosmological models. As in previous works, we assume Gaussian initial conditions and that the linear growth of perturbations is scale-independent. Perturbations are defined, as usual, in term of the matter density contrast $\delta(\mathbf{x}, a) \equiv \rho(\mathbf{x}, a)/\rho_0 - 1$, where $\rho(\mathbf{x}, a)$ is the matter energy density, ρ_0 its background value and a is the scale factor, adopted here as our time variable. We further define the rescaled velocity divergence

$$\theta(\mathbf{x}, a) \equiv -\frac{\partial_i v^i(\mathbf{x}, a)}{f(a)\mathcal{H}(a)}, \quad (1)$$

with $v^i(\mathbf{x}, a)$ being the peculiar matter velocity and $\mathcal{H} = aH(a)$ the conformal Hubble rate. We have introduced the linear growth rate

$$f(a) = \frac{d \log D(a)}{d \log a}, \quad (2)$$

where $D(a)$ is the usual linear growth factor, defined as $\delta_{\text{lin}}(\mathbf{x}, a) = D(a)/D(a_{\text{in}}) \delta_{\text{lin}}(\mathbf{x}, a_{\text{in}})$. We also consider the number density contrast of galaxies,

$$\delta_g(\mathbf{x}, a) = \frac{n_g(\mathbf{x}, a)}{\bar{n}_g} - 1, \quad (3)$$

where \bar{n}_g is the galaxy mean number density. These fields can be expressed as an expansion according to the standard perturbative ansatz [29]

$$\delta(\mathbf{x}, a) = \sum_{n=1}^{\infty} \delta^{(n)}(\mathbf{x}, a), \quad \theta(\mathbf{x}, a) = \sum_{n=1}^{\infty} \theta^{(n)}(\mathbf{x}, a), \quad \delta_g(\mathbf{x}, a) = \sum_{n=1}^{\infty} \delta_g^{(n)}(\mathbf{x}, a). \quad (4)$$

In Fourier space, these expansions can be expressed in terms of convolutions

$$\delta^{(n)}(\mathbf{k}, a) = \int \frac{d^3 q_1}{(2\pi)^3} \cdots \int \frac{d^3 q_n}{(2\pi)^3} (2\pi)^3 \delta_D(\mathbf{k} - \mathbf{q}_{1\dots n}) F_n(\mathbf{q}_1, \dots, \mathbf{q}_n; a) \delta^{(1)}(\mathbf{q}_1; a) \cdots \delta^{(1)}(\mathbf{q}_n; a), \quad (5)$$

$$\theta^{(n)}(\mathbf{k}, a) = \int \frac{d^3 q_1}{(2\pi)^3} \cdots \int \frac{d^3 q_n}{(2\pi)^3} (2\pi)^3 \delta_D(\mathbf{k} - \mathbf{q}_{1\dots n}) G_n(\mathbf{q}_1, \dots, \mathbf{q}_n; a) \delta^{(1)}(\mathbf{q}_1; a) \cdots \delta^{(1)}(\mathbf{q}_n; a), \quad (6)$$

$$\delta_g^{(n)}(\mathbf{k}, a) = \int \frac{d^3 q_1}{(2\pi)^3} \cdots \int \frac{d^3 q_n}{(2\pi)^3} (2\pi)^3 \delta_D(\mathbf{k} - \mathbf{q}_{1\dots n}) K_n(\mathbf{q}_1, \dots, \mathbf{q}_n; a) \delta^{(1)}(\mathbf{q}_1; a) \cdots \delta^{(1)}(\mathbf{q}_n; a). \quad (7)$$

In the standard approach, the convolution kernels F_n , G_n , and K_n are obtained by iteratively solving the continuity and Euler equations for a chosen cosmological model (their explicit expressions are given in Appendix A). In the bootstrap approach, by contrast, the analytic form of these kernels is constrained by imposing symmetry principles, which leave a finite number of time- and cosmology-dependent undetermined functions. For the matter and velocity kernels, we impose constraints that enforce rotational invariance, conservation of mass and momentum, and invariance under time-dependent spatial translations (the so-called extended Galilean invariance which, when combined with the adiabaticity of long-wavelength modes, is equivalent to the Equivalence Principle (EP)). In addition, we require perturbativity, namely that the kernels are built from products of external momentum invariants, with the only permissible poles taking the form \mathbf{q}_i/q_i^2 (for more details, see [8]).

As a result, at second order, the symmetric matter and velocity kernels take the form

$$F_2(\mathbf{q}_1, \mathbf{q}_2; a) = \beta(\mathbf{q}_1, \mathbf{q}_2) + \frac{a\gamma^{(2)}(a)}{2} \gamma(\mathbf{q}_1, \mathbf{q}_2), \quad (8)$$

$$G_2(\mathbf{q}_1, \mathbf{q}_2; a) = \beta(\mathbf{q}_1, \mathbf{q}_2) + \frac{d\gamma^{(2)}(a)}{2} \gamma(\mathbf{q}_1, \mathbf{q}_2), \quad (9)$$

where the mode-coupling functions are defined as

$$\beta(\mathbf{q}_1, \mathbf{q}_2) = \frac{|\mathbf{q}_1 + \mathbf{q}_2|^2 \mathbf{q}_1 \cdot \mathbf{q}_2}{2q_1^2 q_2^2}, \quad (10)$$

$$\gamma(\mathbf{q}_1, \mathbf{q}_2) = 1 - \frac{(\mathbf{q}_1 \cdot \mathbf{q}_2)^2}{q_1^2 q_2^2}. \quad (11)$$

The coefficients of $\beta(\mathbf{q}_1, \mathbf{q}_2)$ are fixed to one by the EP, whereas the undetermined, time-dependent coefficients $a_\gamma^{(2)}$ and $d_\gamma^{(2)}$ that appear in (8) and (9) carry information about the underlying cosmological model. Once a specific model is chosen, these functions can be derived from their equations of motion; for example, in Λ CDM they are given by [7]

$$\frac{da_\gamma^{(2)}(a)}{d \ln a} = f \left(2 - 2a_\gamma^{(2)} + d_\gamma^{(2)} \right), \quad (12)$$

$$\frac{dd_\gamma^{(2)}(a)}{d \ln a} = f \left(\frac{3}{2} \frac{\Omega_m}{f^2} (a_\gamma^{(2)} - d_\gamma^{(2)}) - d_\gamma^{(2)} \right). \quad (13)$$

The PT kernels for biased tracers, the K_n 's, can be obtained in an analogous way to the matter case, with the crucial difference that mass and momentum conservation are not enforced. Because of this, the K_n kernels involve a larger set of independent coefficients than the corresponding matter and velocity kernels at the same perturbative order. Moreover, since the residual symmetries (EP and rotational invariance) coincide with those used in constructing the bias expansion [30], the bootstrap coefficients for biased tracers are completely degenerate with the bias parameters themselves. They therefore cannot be used to recover any cosmological information, i.e., information that is independent of the tracer. As a result, within the bootstrap framework, cosmological constraints arise solely from the velocity sector through redshift-space distortions (RSD), via the linear growth rate f , and the quadratic perturbative parameter $d_\gamma^{(2)}$.

In general, more bootstrap terms appear at third order: specifically $d_{\gamma a}^{(3)}$, $d_{\gamma b}^{(3)}$ and $a_\gamma^{(2)}$, see appendix A for their definitions. Given a specific model, one would generally expect (correlated) deviations in all these coefficients, not just f and $d_\gamma^{(2)}$. Within the analysis performed in this work, power spectrum at one-loop and bispectrum at tree-level, these terms enter only through the P_{13} term and are expected to be very degenerate with the third order bias parameter. Moreover, our combination of observables is particularly insensitive to such third order bias and bootstrap terms, while it is well suited to constrain second order terms, such as quadratic and tidal bias [18, 19, 21, 22, 31]. For these reasons, we will keep all the third order bootstrap coefficient fixed to their Λ CDM prediction and limit our analysis only to deviations from Λ CDM to linear and quadratic order in the perturbative expansion, $f(a)$ and $d_\gamma^{(2)}(a)$. We introduce the fractional deviation parameters,

$$\varepsilon_f \equiv \frac{f}{f_{\Lambda\text{CDM}}} - 1, \quad \varepsilon_{d_\gamma} \equiv \frac{d_\gamma^{(2)}}{d_{\gamma}^{(2), \Lambda\text{CDM}}} - 1, \quad (14)$$

where the dependence of the Λ CDM quantities in the denominators on Ω_m , given by Eq. (13), is taken into account. Any detected non-zero value of ε_f or ε_{d_γ} would therefore signal new physics beyond Λ CDM, which cannot be reabsorbed by merely adjusting Ω_m . By including $d_\gamma^{(2)}$, we probe deviations from Λ CDM in the nonlinear regime, thereby extending the analysis past the linear parameter f and enhancing our ability to distinguish among different beyond- Λ CDM scenarios. As emphasized in previous work [12], extensions of Λ CDM within modified gravity or evolving dark energy scenarios can lead to distinct signatures: models that primarily modify the background expansion, such as those involving non-standard dark energy evolution, mostly affect the time dependence of growth function, resulting in a non-zero ε_f , while leaving the nonlinear evolution of perturbations largely unchanged, i.e. $\varepsilon_{d_\gamma} \simeq 0$. In contrast, modified gravity models typically alter both the background dynamics and the growth of nonlinear structure, leading to a characteristic signal with $\varepsilon_{d_\gamma} \neq 0$. This framework therefore provides a model-independent way to disentangle modifications to the background evolution, encoded in ε_f , from those affecting nonlinear growth, described by ε_{d_γ} , thereby clarifying the theoretical requirements that viable extensions of Λ CDM must satisfy.

To connect the model-independent deviations ε_f and ε_{d_γ} with observables, the galaxy power spectrum and bispectrum are modeled using the EFTofLSS [14, 15], following the implementation in PyBird [17], modified to include the bootstrap framework and the time-dependence of the kernels. The explicit form for the observables is given in Appendix B.

We apply the Alcock-Paczynski (AP) effect [32] as implemented in PyBird to all the analyses (see [22] for details).

III. Datasets and tests

In this section, we describe the datasets and methodology employed to constrain the model-independent parameters ε_f and ε_{d_γ} , using both observational data and numerical simulations.

A. BOSS analysis

We analyze the redshift-space monopole, quadrupole and hexadecapole of the power spectrum, together with the monopole of the bispectrum of the SDSS III BOSS DR12 luminous red galaxies (LRG) sample at redshifts $z = 0.32$ (LOWZ) and $z = 0.57$ (CMASS) [27, 33], using data from both the Northern (NGC) and the Southern (SGC) Galactic Caps.

Computing the power spectrum at the central value of each wavenumber bin, instead of averaging it over the full bin width, has a negligible effect for BOSS. We therefore disregard this difference for the BOSS data, in contrast to the PT Challenge data (see below). For the bispectrum, we adopt the same binning strategy as in [22]. We estimate the covariance matrix, following [22], for the power spectrum, the bispectrum and their cross correlation using Patchy mock catalogs [34]. This catalog consists of 2048 simulated realizations built using the halo occupation distribution (HOD) algorithm in order to match the BOSS galaxy clustering and the different selection functions for each redshift bin. The covariance matrices are estimated using the usual expression

$$\text{Cov}(O_\ell(m_i)O_{\ell'}(m_j)) = \frac{1}{N_{\text{sims}} - 1} \sum_{n=1}^{N_{\text{sims}}} [O_\ell^{(n)}(m_i) - \bar{O}_\ell(m_i)][O_{\ell'}^{(n)}(m_j) - \bar{O}_{\ell'}(m_j)], \quad (15)$$

where $O = \{P, B\}$ are the observables for which we estimate the covariance, $m_i = \{k_i, t_i\}$, respectively the i -th k -bin and the i -th triangular bin. N_{sims} is the total number of simulations, the superscript (n) indicates the measured multipole of the n -th realization and the average is defined as

$$\bar{O}_\ell(m) \equiv \frac{1}{N_{\text{sims}}} \sum_{n=1}^{N_{\text{sims}}} O_\ell^{(n)}(k). \quad (16)$$

B. PT Challenge simulations

We also analyze the redshift-space power spectrum and bispectrum monopole and quadrupole of the ‘PT Challenge’ simulations [28]. They consist of ten realizations in periodic comoving boxes, with a combined volume of $566 (h^{-1} \text{Gpc})^3$. This corresponds to a volume roughly two orders of magnitude larger than that of the BOSS catalogs and about $O(10)$ times greater than that probed by Stage IV surveys. The simulations adopt a flat Λ CDM cosmology, allowing us to carry out null tests of the bootstrap parameters (14). This enables us to evaluate both the constraining power of an ideal, extremely large-volume survey that is free from real-world systematic effects, and the robustness of our methodology.

Dark matter halos are populated using the halo occupation distribution (HOD) technique, matched to reproduce the observed clustering properties of the BOSS samples, in particular the monopole moment of the power spectrum. In this work, we focus on a snapshot at redshift $z = 0.61$, that matches the properties of the ‘high- z ’ BOSS data sample.

In contrast to the BOSS analysis, the substantially smaller uncertainties of the PT Challenge simulations make the effect of binning of the power spectrum non-negligible. We therefore account for this effect as prescribed by the *West Coast team* in [28]. As for the bispectrum, we consider triangles whose sides start from the fundamental frequency $k_f = 0.005 h \text{Mpc}^{-1}$, and are binned with a linear spacing of width $\Delta k = 2k_f$.

The power spectrum covariance matrix is supplied with the data and is computed under the assumption of Gaussianity, following the methodology of [28], separately for each of the ten realizations. For the analysis of the total volume spanned by the ten boxes, we combine these ten individual covariance matrices into a single covariance via a weighted average.

The covariance matrix for the bispectrum is estimated as described in App. D. We neglect the cross-covariance between the power spectrum and bispectrum, as it has been shown to be negligible at the scale cuts adopted in this work (see, e.g., [18, 19, 21, 35, 36]). However, we include the correlations between different bispectrum multipoles, as done for the power spectrum multipoles P_ℓ .

C. Parameters and priors

We perform MCMC analyses using the Metropolis–Hastings algorithm as implemented in `MontePython 3` [37, 38], numerically sampling the parameter set

$$\{\omega_b, \omega_{cdm}, h, \ln(10^{10} A_s), \varepsilon_f, \varepsilon_{d_\gamma}, b_1, b_2, b_4\}. \quad (17)$$

We follow the `PyBird` [17] convention for the quadratic bias parameters b_2 and b_4 ; see also Eq. (E11) for their mapping to alternative bases. We impose flat priors on all parameters except for the baryonic density ω_b (see below) and the primordial scalar amplitude A_s . Since A_s exhibits strong degeneracies (see Sect. III E), we consider three different treatments:

1. we leave it free (only for the BOSS analysis);
2. we fix $\ln(10^{10}A_s) = 3.0448$, the *Planck* best-fit value [39], for the BOSS analysis, and to the true value used in the simulations for the PT Challenge;
3. we instead adopt a Gaussian prior on A_s with a width equal to 3σ of the *Planck* uncertainty [39], following refs. [40, 41].

Given that *Planck*'s uncertainty on A_s is extremely small, fixing A_s or applying a 3σ Gaussian prior leads to nearly identical constraints, as demonstrated in App. C.

The BOSS data are split into two separate redshift samples, and the model-independent parameters ε_f and ε_{d_γ} are in general time-dependent. We therefore treat them as independent in each redshift bin, obtaining two sets of bootstrap parameters per redshift:

$$\{\varepsilon_f^l, \varepsilon_{d_\gamma}^l, \varepsilon_f^h, \varepsilon_{d_\gamma}^h\}, \quad (18)$$

where the superscripts l and h denote the LOWZ and CMASS samples, respectively. The bias parameters (b_1, b_2, b_4) are treated as independent for each redshift bin and sky region (NGC and SGC), resulting in four sets of bias parameters. Conversely, the cosmological parameters are assumed to be shared across both bins and sky regions.

Adopting the notation of [42, 43], we perform an analytic marginalization over the following bias and EFT parameters that appear in the theoretical model (see Appendix B for details):

$$\{c_{\text{ct},1}, c_{\text{ct},2}, c_{\text{ct},3}, c_{\text{ct},4}, c_{\varepsilon,0}, c_{\varepsilon,1}, c_{\varepsilon,\text{quad}}, c_{\varepsilon,3}, c_{\varepsilon,4}, \tilde{b}_3, \tilde{b}_8\} \quad (19)$$

where we have defined the following combination of parameters:

$$c_{\varepsilon,\text{quad}} = \frac{2}{3}f c_{\varepsilon,2}, \quad c_{\text{ct},1} = -c_{\text{ct}}, \quad c_{r,1} = c_{\text{ct},2}f - \frac{1}{2}f^2 c_{\text{ct},4}, \quad c_{r,2} = -\frac{1}{2}c_{\text{ct},3}f^2, \quad b_3 = \tilde{b}_3 + 15 \tilde{b}_8. \quad (20)$$

The mapping between the parameters adopted in this work and those used in `PyBird` can be found in Appendix D4 of [42]. In our BOSS data analysis we fix the scalar spectral index to the *Planck* best-fit value, $n_s = 0.96605$, since the data are not very sensitive to it. We apply a Gaussian prior on the baryon density, $\omega_b = 0.022445 \pm 0.00038$, as inferred from Big Bang Nucleosynthesis [39]. For the PT Challenge analysis, we hold the spectral index fixed at the fiducial value used in the simulations, $n_s = 0.9649^1$, and apply a Gaussian prior on the baryon density ω_b , again centered on the fiducial value adopted in the simulations with the BBN width, 0.00038.

For the strong-coupling scale k_M (see Appendix B) we adopt the value $k_M = 0.7 h \text{ Mpc}^{-1}$. The galaxy number density is set to $\bar{n}_g = 4 \cdot 10^{-4} (h^{-1} \text{ Mpc})^3$ for BOSS and $\bar{n}_g = 3 \cdot 10^{-4} (h^{-1} \text{ Mpc})^3$ for the PT Challenge simulations. We adopt flat priors on the bootstrap parameters

$$\begin{aligned} \varepsilon_f &\in [-2, 2], \\ \varepsilon_{d_\gamma} &\in [-2, 2], \end{aligned} \quad (21)$$

and Gaussian priors on all bias and EFT parameters, as listed in Table I.

Overall, our choice of priors largely mirrors those adopted in earlier `PyBird` analyses [22, 28, 43, 44]. The only departure concerns the stochastic parameters in the PT Challenge analysis. In the PT Challenge data provided to us, the shot noise has been removed from the power spectrum but not from the bispectrum. To maintain consistency between the two, we reintroduced the shot-noise term into the power spectrum monopole. Specifically, we estimated the mean number density in each simulation box via

$$\frac{1}{\bar{n}} = \frac{L^3}{N_{\text{gal}}} \quad (22)$$

with $L = 3840 h^{-1} \text{ Mpc}$ denoting the box size and N_{gal} the number of mock galaxies in the box. We then averaged $1/\bar{n}$ over the 10 boxes and added this constant shot-noise correction to the power spectrum monopole in every k -bin. Since we explicitly restore the $1/\bar{n}$ contribution to the power spectrum monopole, we shift the prior on the associated stochastic nuisance parameters $c_{\varepsilon,0}, c_{\varepsilon,3}, c_{\varepsilon,4}$, as defined in Appendix B, to be centered on 1 rather than 0.

We declare the convergence of the MCMC's when the Gelman-Rubin $R - 1$ value [45] is ≤ 0.03 for all sampled parameters. All our plots are generated using the `GetDist` package [46].

¹ See the [PT Challenge website](#) for details

Parameter	Prior (PT Challenge)	Prior (BOSS)
b_1	Lognormal(0.8, 0.8)	-
b_2	$\mathcal{N}(0, 2)$	-
b_4	$\mathcal{N}(0, 2)$	-
\tilde{b}_3	$\mathcal{N}(0, 2)$	-
\tilde{b}_8	$\mathcal{N}(0, 2)$	-
$c_{\text{ct},1}$	$\mathcal{N}(0, 4)$	-
$c_{\text{ct},2}$	$\mathcal{N}(0, 4)$	-
$c_{\text{ct},3}$	$\mathcal{N}(0, 4)$	-
$c_{\text{ct},4}$	$\mathcal{N}(0, 4)$	-
$c_{\epsilon,0}$	$\mathcal{N}(1, 0.2)$	$\mathcal{N}(0, 0.2)$
$c_{\epsilon,1}$	$\mathcal{N}(0, 4)$	-
$c_{\epsilon,\text{quad}}$	$\mathcal{N}(0, 2)$	-
$c_{\epsilon,3}$	$\mathcal{N}(1, 0.4)$	$\mathcal{N}(0, 0.4)$
$c_{\epsilon,4}$	$\mathcal{N}(1, 1)$	$\mathcal{N}(0, 1)$

Table I: List of priors adopted on bias, counterterms, and stochastic parameters. $\mathcal{N}(\mu, \sigma)$ represents a normal distribution with mean μ and standard deviation σ . A log-normal prior is adopted for b_1 , implemented as a Gaussian prior on $\ln b_1$. A dash (-) indicates that the corresponding parameter shares the same prior as in the PT Challenge case.

D. Scale cuts

We do not perform scale-cut tests for the BOSS data, since we adopt the same maximum wavenumbers k_{max} that were already validated in previous PyBird-based analyses of the BOSS DR12 LRG sample [22, 42, 47]. Concretely, we use $k_{\text{max},P_\ell} = 0.20 h \text{ Mpc}^{-1}$ for LOWZ, $k_{\text{max},P_\ell} = 0.23 h \text{ Mpc}^{-1}$ for CMASS, and $k_{\text{max},B_0} = 0.08 h \text{ Mpc}^{-1}$ for the bispectrum monopole in both samples.

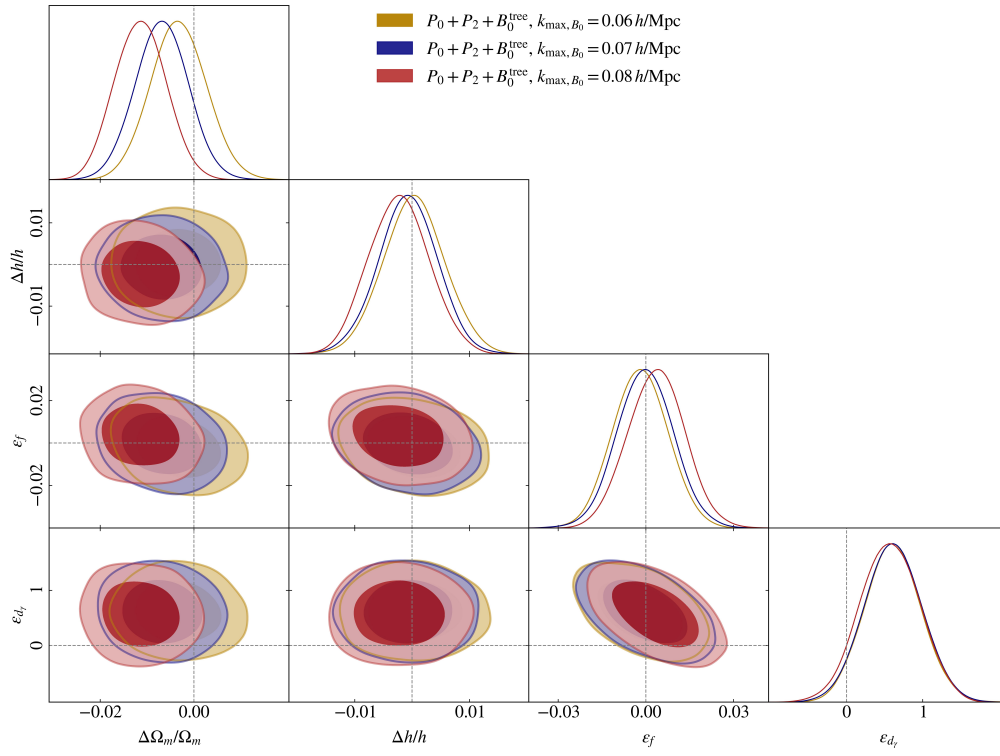
For the PT Challenge simulations, following the arguments in [28], we analyze the power spectrum multipoles up to $k_{\text{max}} = 0.14 h \text{ Mpc}^{-1}$. In contrast, for the bispectrum multipoles we explicitly test different values of k_{max} , denoted k_{max,B_0} and k_{max,B_2} for the monopole and quadrupole, respectively. These tests are carried out using the parameter set and priors specified in Sec. III C, while fixing the primordial scalar amplitude A_s to the true value adopted in the simulations.

Figure 1a shows the effect of raising k_{max,B_0} from 0.06 to 0.08 $h \text{ Mpc}^{-1}$. Increasing this cut leads to shifts in the posterior means of the ϵ -parameters, but these remain well within their corresponding 1σ statistical errors. In contrast, the inferred value of Ω_m shifts by more than 1σ once k_{max,B_0} exceeds 0.07 $h \text{ Mpc}^{-1}$, signaling the growing importance of 1-loop contributions, as discussed below.

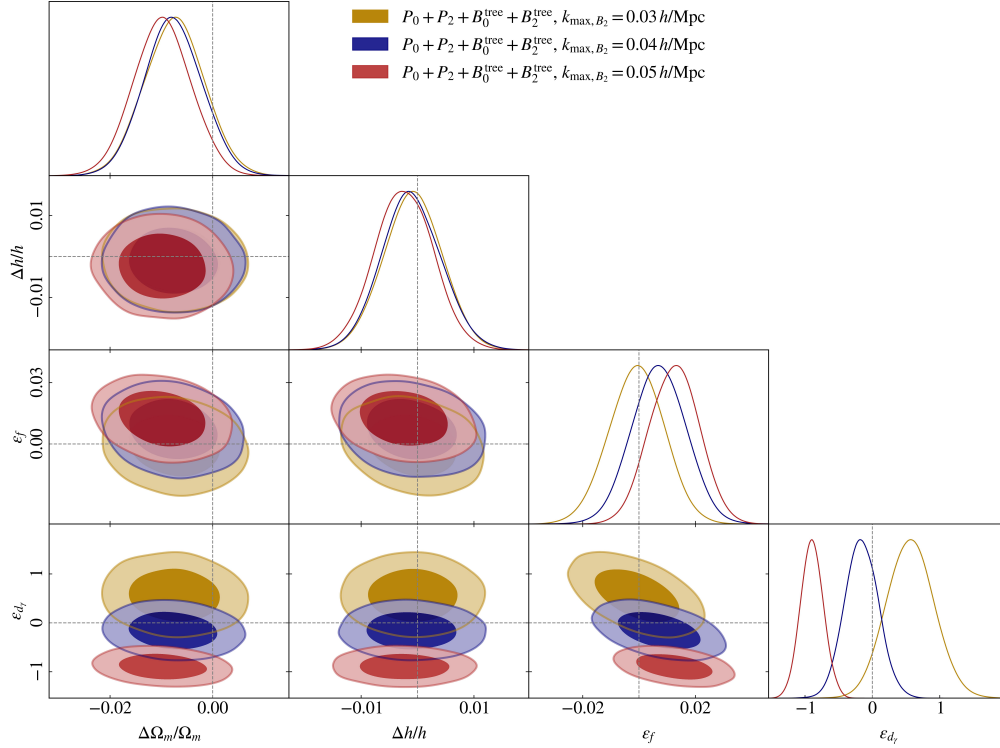
In Fig. 1b, we extend the analysis to include the bispectrum quadrupole, fix $k_{\text{max},B_0} = 0.07 h \text{ Mpc}^{-1}$, and examine how varying k_{max,B_2} impacts the results. We find that changing k_{max,B_2} has only a modest effect on the cosmological parameters and on ϵ_f , but it more noticeably alters the posterior of ϵ_{d_γ} . This pattern emerges because, as k_{max} increases, 1-loop corrections and non-linear redshift-space distortions degrade the accuracy of our tree-level bispectrum description. This is illustrated in Fig. 2, where we compare ΛCDM analyses that include the 1-loop prediction for the bispectrum monopole and quadrupole with those based solely on the tree-level bispectrum multipoles, for $k_{\text{max},B_2} = 0.04 h \text{ Mpc}^{-1}$ (left panel) and $k_{\text{max},B_2} = 0.05 h \text{ Mpc}^{-1}$ (right panel).

Conversely, lowering k_{max,B_2} below 0.04 $h \text{ Mpc}^{-1}$ significantly shrinks the number of usable triangular configurations, effectively removing the bispectrum quadrupole from the analysis. This can be verified by comparing the ϵ_{d_γ} contours obtained for $k_{\text{max},B_2} = 0.03 h \text{ Mpc}^{-1}$ in Fig. 1b with those shown in Fig. 1a.

Taking all these results into account, we adopt $k_{\text{max},B_0} = 0.07 h \text{ Mpc}^{-1}$ and $k_{\text{max},B_2} = 0.04 h \text{ Mpc}^{-1}$ as our baseline choices for the PT Challenge analysis, as they provide a conservative yet unbiased setup for our tree-level bispectrum modeling.



(a) Posteriors as a function of k_{\max, B_0} for the PT Challenge simulations.



(b) Posteriors as a function of k_{\max, B_2} for the PT Challenge simulations. In all cases, we fix $k_{\max, B_0} = 0.07 h \text{ Mpc}^{-1}$.

Figure 1: Impact of the choice of k_{\max} on the posterior distributions for the PT Challenge simulations for the bispectrum monopole B_0 (top panel) and quadrupole B_2 (bottom panel). Both analyses are performed with n_s and A_s fixed to the true values of the simulations.

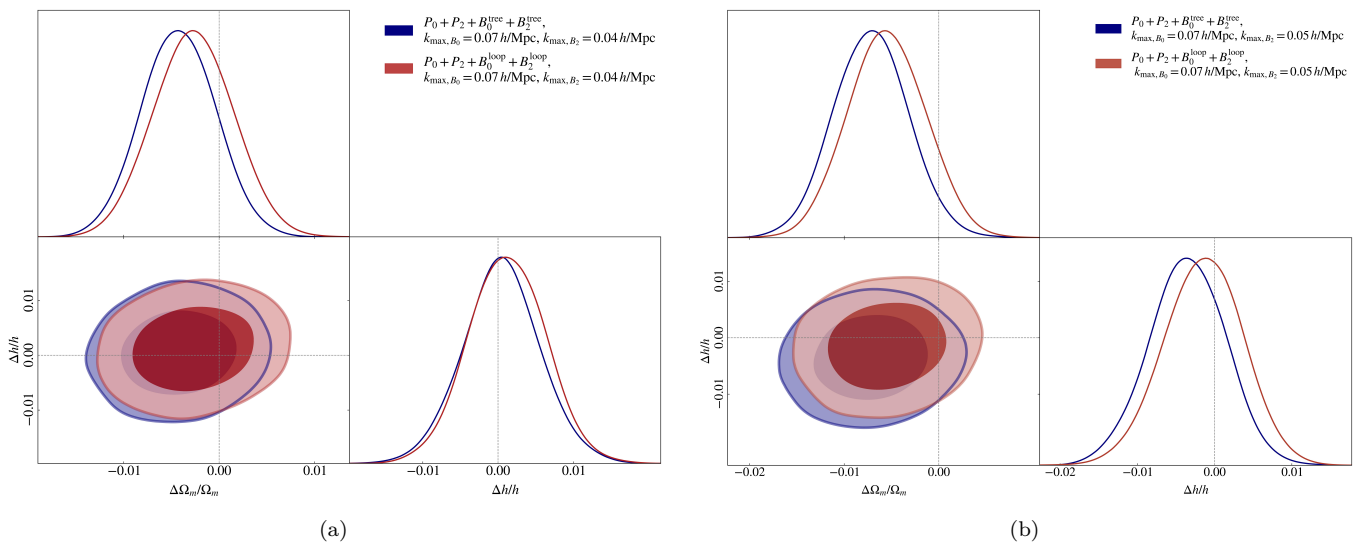


Figure 2: Impact of the 1-loop bispectrum (red) on cosmological constraints with respect to the tree-level contribution (blue). Analyses are performed at fixed cosmology (Λ CDM), with n_s and A_s fixed to the true values of the simulations.

E. Degeneracies

In this section, we examine the parameter degeneracies that impact our analysis. At linear order, it is well known that the amplitude of primordial scalar fluctuations, A_s , is completely degenerate with the linear galaxy bias, b_1 . This degeneracy is broken in redshift space, in absence of strong observational effects [48], assuming a perfect knowledge of the growth function f . Leaving f free to vary in the model, as we do in this work in the spirit of a model-agnostic analysis, will restore the broken degeneracy, and cause possible projection effects in the parameter posterior. As shown in Fig. 3, the degeneracies among b_1 , A_s and f are partially broken once nonlinear effects are taken into account, both through the 1-loop corrections to the power spectrum and through the inclusion of the bispectrum, as well as by exploiting information from redshift-space anisotropies, including higher-order multipoles.

Nonetheless, when all three parameters are allowed to vary simultaneously, projections along these degenerate directions in parameter space yield posterior distributions that are shifted relative to the fiducial values. This behavior is a generic feature of models beyond Λ CDM, as previously emphasized in [41, 44, 49, 50].

To quantify these projection effects, following [49], we compare the MAP values obtained from minimization with the 68%-credible intervals in Fig. 3. As shown in Fig. 4, the inclusion of bispectrum multipoles, compared to the power spectrum only case, provides only a marginal reduction of the projection effects on A_s , b_1 and ε_f , which remain large even when including the bispectrum quadrupole B_2 ($\sim 4.23\sigma$, 3.78σ and 3.61σ , respectively). This confirms that the A_s - b_1 - ε_f degeneracy cannot be resolved by the bispectrum multipoles alone.

Since the main objective of our work is to constrain signatures of new physics, rather than to perform a full Λ CDM analysis based solely on galaxy clustering, we fix A_s to the true value used in the PT Challenge simulations. This prescription effectively mimics the inclusion of external information from complementary probes, such as the CMB, as also shown in Appendix C. Accordingly, in what follows we present results with A_s fixed to the true value of the PT Challenge, a choice that guarantees convergence and enables a robust inference of cosmological, bias, and model-independent parameters.

In contrast to ε_f , the bootstrap parameter ε_{d_γ} does not show significant degeneracies with the cosmological parameters, but it is degenerate with the quadratic bias coefficients b_2 and b_4 . This can be understood by looking at Eq. (E11), which shows the relation between $b_{2,4}$ and b_{K^2} , and noticing the relation between γ and K^2 is $\gamma(\mathbf{q}_1, \mathbf{q}_2) = 2/3 - K^2(\mathbf{q}_1, \mathbf{q}_2)$. This means that a better knowledge of higher order bias parameters (second order in this specific case) will substantially increase the sensitivity to ε_{d_γ} . This is what we observe in our analysis: including the bispectrum quadrupole improves the constraints on this beyond- Λ CDM parameter. In particular, the projection effects on ε_{d_γ} decrease from 1.76σ ($P_0 + P_2 + B_0$) to 0.14σ ($P_0 + P_2 + B_0 + B_2$), and a similar reduction is observed for the bias parameter b_4 (from 2.31σ to 1.43σ), consistently with the degeneracy between ε_{d_γ} and the quadratic bias parameters discussed above. Consequently, the bootstrap parameter ε_{d_γ} can be tightly constrained even without fixing the amplitude of primordial scalar fluctuations, A_s , making it a robust probe of new physics beyond Λ CDM. In contrast, the projection effects on b_2 remain large even with the inclusion of the bispectrum quadrupole, since b_2 is strongly correlated with b_1 through

Eq. (E11).

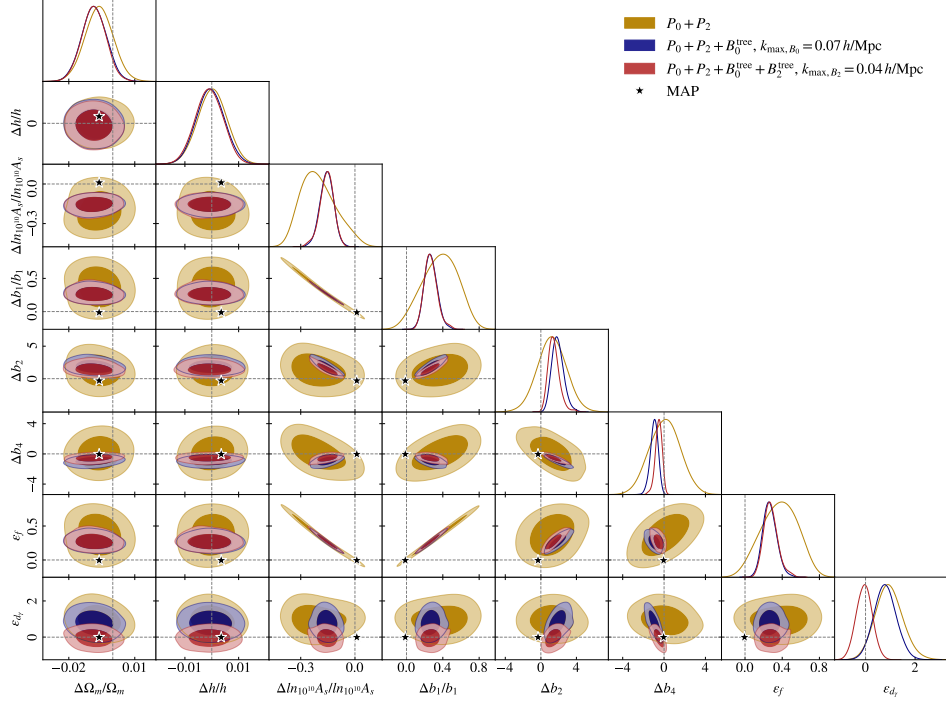


Figure 3: Posteriors for the PT Challenge simulations, with n_s fixed to the true value and A_s varied with a flat prior. We adopt $k_{\max, B_0} = 0.07 h \text{ Mpc}^{-1}$ and $k_{\max, B_2} = 0.04 h \text{ Mpc}^{-1}$. Dashed lines represent the fiducial values of the simulations for the cosmological and bootstrap parameters, and the inferred values for the bias ones (see Appendix E for details). The shifts of the posteriors with respect to dashed lines indicate biased results when ε_f , A_s and b_1 are allowed to vary simultaneously. Stars indicate the MAP values obtained from minimization.

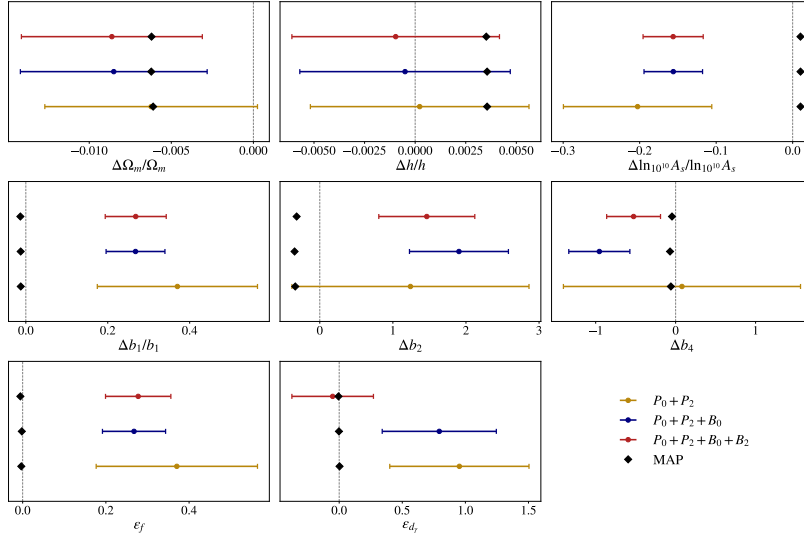


Figure 4: Posterior means and 1σ intervals (colored bars) and MAP values, denoted by black diamond markers, for the PT Challenge simulations, with A_s free. Projection effects are reflected in the discrepancies between the MAP values and the maxima of the marginalized posterior distributions.

In the BOSS analysis, the degeneracies are less pronounced because of the smaller survey volume and the correspondingly broader constraints. For this reason, in this case we show results both allowing A_s to vary and keeping it fixed; see Sect. IV A and Fig. 5.

IV. Results

A. BOSS analysis

1. A_s free

Figure 5a shows the marginalized posterior distributions of the cosmological and bootstrap parameters for the BOSS LOWZ and CMASS samples, with the corresponding constraints summarized in the upper block of Table II.

The power spectrum multipoles on their own do not offer enough constraining power to jointly determine the cosmological parameters and the new model-independent parameters ε_f and ε_{d_γ} . As highlighted in the previous section, the strong degeneracy between ε_f and A_s induces projection effects and biased constraints, preventing us from recovering values consistent with those derived from *Planck* data [39].

For this reason, incorporating the bispectrum is essential: it greatly enhances both the precision and the overall constraining ability of the analysis. This agrees with earlier works that combine power spectrum and bispectrum (P+B) [19, 21, 22, 36, 40, 41], which have shown that the bispectrum provides extra constraining power, helping to break parameter degeneracies and reduce projection effects.

Focusing on the bootstrap parameters, we observe that incorporating the bispectrum leads to posterior distributions of ε_f that are consistent with its Λ CDM prediction and decreases its uncertainty from 0.24 to about 0.135 in LOWZ and from 0.16 to 0.097 in CMASS, corresponding to reductions of 44% and 39%, respectively. The parameter ε_{d_γ} is already in agreement with Λ CDM when only the power spectrum is considered; nonetheless, adding the bispectrum monopole further sharpens its constraints, cutting the uncertainty from 1.3 in both redshift bins down to 0.69 (LOWZ) and 0.68 (CMASS), which represents an improvement of roughly 47%.

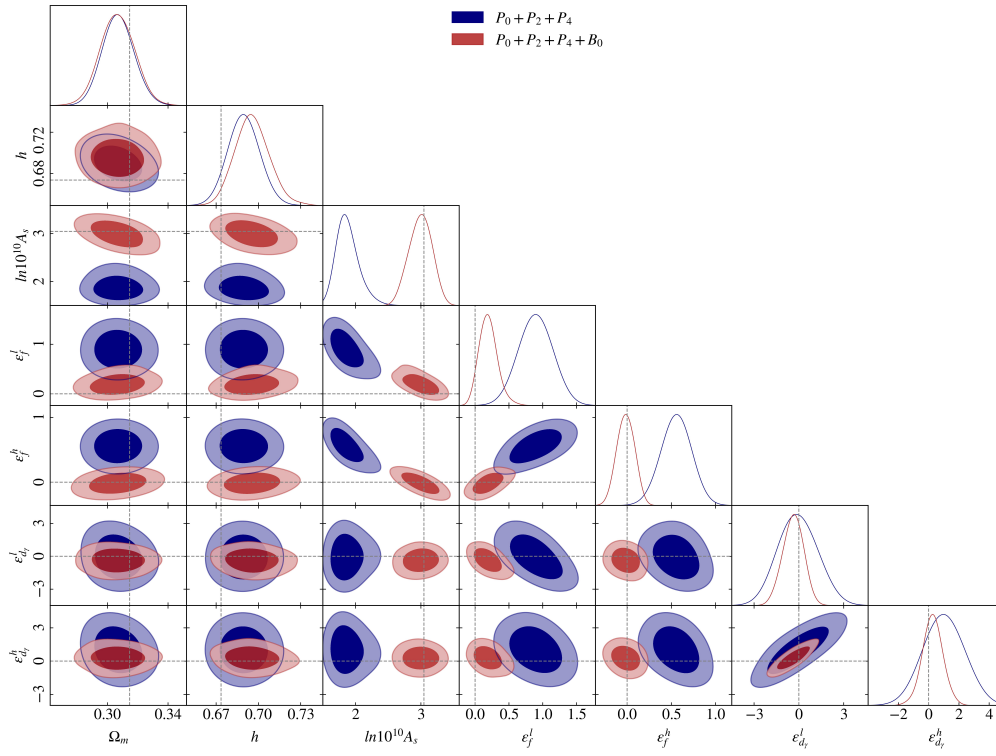
2. A_s fixed

We re-ran the BOSS analysis with A_s fixed to the *Planck* best-fit value [39]. This choice enables a consistent comparison between the BOSS and PT Challenge results and demonstrates how a joint analysis of data from forthcoming galaxy surveys together with external datasets can further tighten current constraints on model-independent parameters.

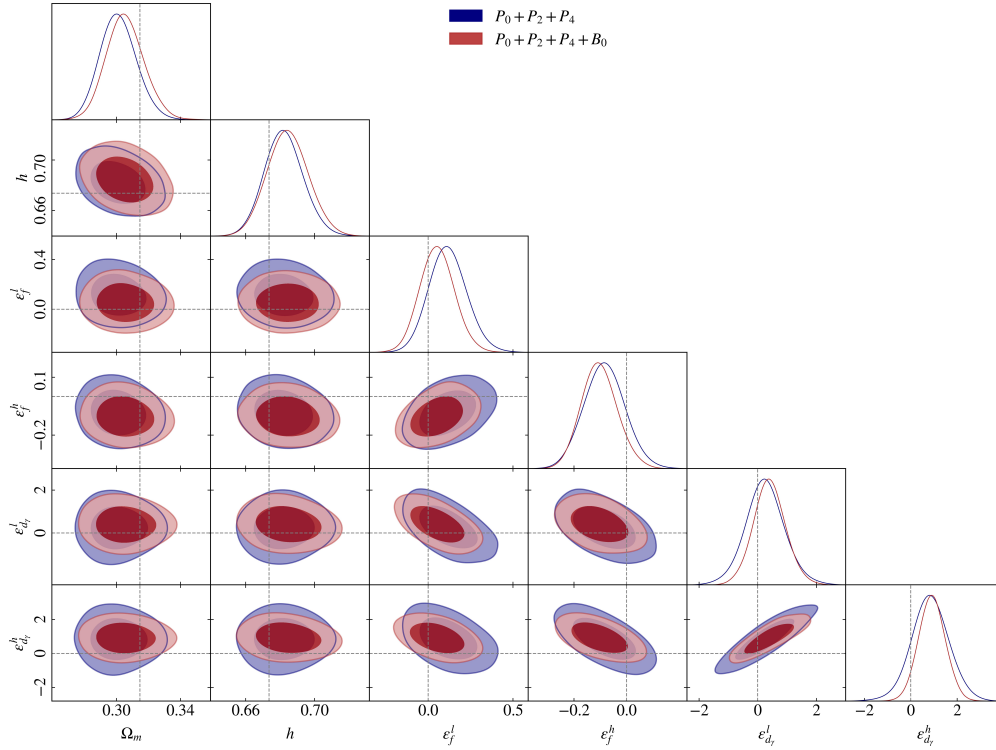
As illustrated in Fig. 5b, when A_s is held fixed, the bispectrum does not add substantial constraining power beyond that of the power spectrum alone. It does, however, lead to a modest tightening of the bootstrap parameter bounds. In particular, the uncertainties on ε_f are further reduced by about 25% for LOWZ and 20% for CMASS, while those on ε_{d_γ} decrease by roughly 20%. The corresponding parameter constraints are reported in the lower block of Table II.

	Dataset	Ω_m	h	$\ln(10^{10}A_s)$	ε_f		ε_{d_γ}	
					LOWZ	CMASS	LOWZ	CMASS
A_s free	P_l	0.3071 ± 0.0099	0.690 ± 0.011	$1.87^{+0.14}_{-0.19}$	0.90 ± 0.24	0.56 ± 0.16	-0.1 ± 1.3	1.0 ± 1.3
	$P_l + B_0$	0.307 ± 0.011	$0.696^{+0.011}_{-0.013}$	$3.00^{+0.19}_{-0.17}$	$0.19^{+0.12}_{-0.15}$	-0.015 ± 0.097	-0.38 ± 0.69	0.27 ± 0.68
A_s fixed	P_l	$0.301^{+0.011}_{-0.012}$	$0.682^{+0.011}_{-0.012}$	–	$0.12^{+0.10}_{-0.12}$	-0.084 ± 0.078	0.25 ± 0.67	0.84 ± 0.82
	$P_l + B_0$	$0.306^{+0.011}_{-0.012}$	0.685 ± 0.012	–	0.05 ± 0.10	$-0.103^{+0.064}_{-0.072}$	0.40 ± 0.54	0.91 ± 0.57

Table II: Constraints on cosmological and model-independent parameters derived from the BOSS LOWZ and CMASS samples. Top panel: A_s allowed to vary. Bottom panel: A_s held fixed. The cosmological parameters are common to both redshift bins, whereas the model-independent parameters ε_f and ε_{d_γ} , which depend on time, are fit separately for each sample. The quoted values are posterior means with 68% confidence intervals.



(a)



(b)

Figure 5: Marginalized posterior distributions for the BOSS LOWZ and CMASS datasets with n_s fixed to *Planck* best-fit and a flat prior on A_s (top panel) and A_s fixed to *Planck* central value (bottom panel). Dashed lines represent the best-fit values from *Planck* [39].

B. PT Challenge simulations

The BOSS analysis highlights the advantages of combining the power spectrum with the bispectrum, but the limited survey volume restricts how precisely we can determine the model-independent parameters ε_f and ε_{d_γ} . To assess the potential gains achievable with larger datasets, we therefore turn to the PT Challenge simulations, whose significantly greater volume enables much tighter constraints.

Figure 6 displays the marginalized posterior distributions for the cosmological parameters, and the corresponding numerical constraints are summarized in Table III. When the bispectrum multipoles are included, the constraints on ε_f are only modestly improved relative to those obtained from the power spectrum alone, tightening from about 0.012 to 0.0097. In contrast, adding the bispectrum quadrupole is crucial for obtaining unbiased constraints on ε_{d_γ} , yielding uncertainties at the ~ 0.25 level.

Furthermore, in comparison with the A_s -free analysis shown in Fig. 3, fixing A_s allows us to accurately recover the fiducial PT Challenge values of both the linear bias b_1 , the quadratic biases, b_2 and b_4 ² and the model-independent parameter ε_f .

Relative to the BOSS results, the increase in constraining power provided by the PT Challenge data is dramatic. Since these simulations cover a volume roughly 100 times larger, they reduce the uncertainty on ε_f by a factor of 7, improving the precision from about 0.068 in the high-redshift BOSS sample to 0.01 in the PT Challenge. Additionally, the parameter ε_{d_γ} , which BOSS could only weakly constrain, now has an uncertainty reduced by a factor of about 2.5, down to the ~ 0.25 level.

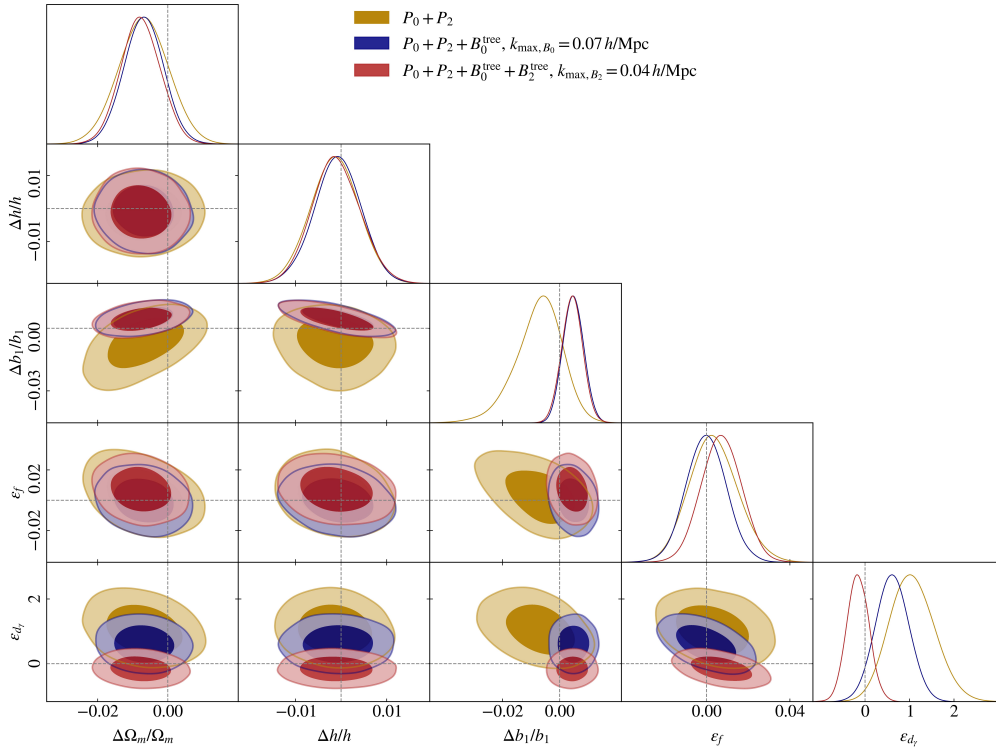


Figure 6: Posteriors for the PT Challenge, with n_s and A_s fixed to the truth of the simulations. We adopt $k_{\max, B_0} = 0.07h \text{ Mpc}^{-1}$ and $k_{\max, B_2} = 0.04h \text{ Mpc}^{-1}$.

² The value of the simulation biases parameter b_1 , b_2 and b_4 have been estimated via the peak-background split approach, as described in Appendix E.

Dataset	$\Delta\Omega_m/\Omega_m$	$\Delta h/h$	ε_f	ε_{d_γ}
P_l	-0.0069 ± 0.0071	-0.0014 ± 0.0054	0.003 ± 0.012	$1.06^{+0.47}_{-0.53}$
$P_l + B_0$	-0.0068 ± 0.0056	-0.0008 ± 0.0052	-0.0002 ± 0.0097	0.61 ± 0.38
$P_l + B_0 + B_2$	-0.0077 ± 0.0057	-0.0011 ± 0.0053	0.0071 ± 0.0097	-0.16 ± 0.25

Table III: Constraints for the PT Challenge simulations, with n_s and A_s fixed. Reported values correspond to posterior means with 68% confidence intervals.

V. Conclusion and outlook

In this work, we have employed a model-independent framework based on the LSS bootstrap to probe departures from the standard Λ CDM picture over a broad class of cosmological models. The primary objective of our study has been to determine how tightly current and forthcoming galaxy clustering measurements can constrain both the linear and nonlinear perturbation sectors, characterized by the bootstrap parameters ε_f and ε_{d_γ} .

By jointly analyzing ε_f , which encodes deviations in the linear growth, and ε_{d_γ} , which describes modifications in the nonlinear evolution, we can alleviate degeneracies between different extensions of the Λ CDM framework. Our study makes use of the `PyBird` code, which we have adapted to consistently incorporate the LSS Bootstrap parametrization and the exact time evolution in the Λ CDM limit. We have implemented this pipeline on both observational data from the BOSS survey and mock data from the large-volume PT Challenge simulations. Using a state-of-the-art P+B analysis, with the power spectrum modeled up to one-loop and the bispectrum multipoles evaluated at tree-level, we obtain constraints on the linear ε_f of ~ 0.07 (0.10) level and on the bootstrap parameter ε_{d_γ} at the ~ 0.57 (0.54) level for the CMASS (LOWZ) samples. For the PT Challenge simulations, we find significantly tighter constraints, reaching the ~ 0.01 level on ε_f and ~ 0.25 on ε_{d_γ} . Our findings underscore the crucial impact of bispectrum multipoles on constraining the nonlinear parameter ε_{d_γ} : in particular, for the PT Challenge dataset, the redshift-space information encoded in the bispectrum quadrupole adds information that tightens the constraints on ε_{d_γ} and also reduces its projection effects.

The marked gains exhibited by the PT Challenge simulations highlight the pivotal role of survey volume in tightening constraints on the bootstrap parameters. However, assuming good control of systematic errors, the ultimate improvement is limited by the reliability of the theoretical framework, most notably the modeling of redshift-space distortions, which sets the minimum scales that can be robustly exploited in the analysis. Accordingly, a natural next step is to include the bispectrum at one-loop order, thereby allowing a self-consistent extension of the analysis to larger values of k_{\max} .

The key question at this stage is whether the current ‘state-of-the-art’ constraints obtained in this work can be sharpened by incorporating information beyond the power spectrum and the (potentially one-loop) bispectrum, either through alternative summary statistics or through fully field-level analyses (see, for example, [51–56]).

An initial step toward realizing field-level inference within the bootstrap framework was presented in [9], which examined the matter distribution in real space for fixed initial conditions. To push this approach further and apply it to actual observations, sophisticated sampling techniques such as Hamiltonian Monte Carlo will be needed to marginalize over both the amplitudes and phases of the linear modes.

We leave these interesting developments for future work.

Acknowledgments

G. Bizelli and M. Pietroni thank the Yukawa Institute for Theoretical Physics (Kyoto), where this work was completed, for hospitality. We thank Takahiro Nishimichi for providing us with the data from the ‘PT Challenge’ simulations and assistance on how to use them, and Matteo Peron for collaborating to the initial stages of this project. We thank Kevin Pardede for useful discussions regarding the calculations of the theoretical covariance.

Numerical computations were performed on the High Performance Computing facility of the University of Parma, Italy, whose support team we thank.

A. Equations of motion and Perturbation Theory Kernels

The Fourier space equations of motion for the dark matter overdensity δ and the velocity divergence θ are given by

$$\begin{aligned}
\partial_\eta \delta_{\mathbf{k}} - f \theta_{\mathbf{k}} &= f \mathcal{I}_{\mathbf{k}, \mathbf{q}_1, \mathbf{q}_2} \alpha(\mathbf{q}_1, \mathbf{q}_2) \theta_{\mathbf{q}_1} \delta_{\mathbf{q}_2} , \\
\partial_\eta \theta_{\mathbf{k}} - f \theta_{\mathbf{k}} + \frac{3}{2} \frac{\Omega_m}{f} \mu_\Phi \theta_{\mathbf{k}} + \frac{1}{f} \frac{k^2}{\mathcal{H}^2} \Phi_{\mathbf{k}} &= f, \mathcal{I}_{\mathbf{k}, \mathbf{q}_1, \mathbf{q}_2} \beta(\mathbf{q}_1, \mathbf{q}_2) \theta_{\mathbf{q}_1} \theta_{\mathbf{q}_2} ,
\end{aligned} \tag{A1}$$

where the time dependence has been omitted to avoid clutter, and we have defined

$$\mathcal{I}_{\mathbf{k}, \mathbf{q}_1, \dots, \mathbf{q}_n} \equiv \int \frac{d^3 \mathbf{q}_1}{(2\pi)^3} \dots \frac{d^3 \mathbf{q}_n}{(2\pi)^3} \delta_D(\mathbf{k} - \mathbf{q}_1 \dots \mathbf{q}_n) , \tag{A2}$$

with $\mathbf{q}_{1\dots n} = \sum_{i=1}^n \mathbf{q}_i$. The functions α and β are the standard dark matter interaction vertices, that describe the non-linear coupling between different modes in the evolution of the density and velocity fields, defined as

$$\alpha(\mathbf{q}_1, \mathbf{q}_2) \equiv \frac{\mathbf{q}_1 \cdot (\mathbf{q}_1 + \mathbf{q}_2)}{q_1^2} , \quad \beta(\mathbf{q}_1, \mathbf{q}_2) \equiv \frac{|\mathbf{q}_1 + \mathbf{q}_2|^2 \mathbf{q}_1 \cdot \mathbf{q}_2}{2q_1^2 q_2^2} . \tag{A3}$$

The time-dependent function $\mu_\Phi(\eta)$ encodes possible linear modifications to the gravitational interaction. General relativity is recovered for $\mu_\Phi = 1$.

The system is closed by the Poisson equation for the gravitational potential Φ , given by

$$-\frac{k^2}{\mathcal{H}^2} \Phi_{\mathbf{k}} = \frac{3}{2} \mu_\Phi \Omega_m \delta_{\mathbf{k}} . \tag{A4}$$

Possible non-linear modifications would enter through higher-order terms.

We proceed by summarizing the explicit expression for the perturbation theory kernels up to third order, following [44]³. The galaxy kernels are

$$K_1(\mathbf{q}_1, a) = b_1 , \tag{A5}$$

$$K_2(\mathbf{q}_1, \mathbf{q}_2, a) = (-b_1 + b_2 + b_4) + b_1 \beta(\mathbf{q}_1, \mathbf{q}_2) + \left(b_1 - \frac{2}{7} b_2 \right) \gamma(\mathbf{q}_1, \mathbf{q}_2) , \tag{A6}$$

$$\begin{aligned}
K_3(\mathbf{q}_1, \mathbf{q}_2, \mathbf{q}_3, a) \Big|_{\text{sub}} &= \frac{b_1}{3} O_{\beta\beta}(\mathbf{q}_1, \mathbf{q}_2, \mathbf{q}_3) + \frac{1}{3} \left(\frac{g(a)b_1}{2} + \frac{b_3}{21} \right) O_{\gamma\beta}(\mathbf{q}_1, \mathbf{q}_2, \mathbf{q}_3) \\
&+ \frac{1}{3} \left(\frac{g(a)b_1}{2} - \frac{b_3}{21} \right) \left(O_{\gamma\gamma}(\mathbf{q}_1, \mathbf{q}_2, \mathbf{q}_3) + \frac{1}{2} O_{\gamma\alpha_a}(\mathbf{q}_1, \mathbf{q}_2, \mathbf{q}_3) \right) + \text{cyclic} ,
\end{aligned} \tag{A7}$$

where the subscript ‘‘sub’’ denotes the subtracted (finite) part of the third-order kernel in the limit $q/k \rightarrow \infty$. This corresponds to the contribution that enters the 1-loop power spectrum (B1) through the particular combination of momenta $K_3(\mathbf{k}, \mathbf{q}, -\mathbf{q})$.

The velocity field kernels are given by

$$G_1(\mathbf{q}_1, a) = 1 , \tag{A8}$$

$$G_2(\mathbf{q}_1, \mathbf{q}_2, a) = \beta(\mathbf{q}_1, \mathbf{q}_2) + \frac{d_\gamma^{(2)}}{2} \gamma(\mathbf{q}_1, \mathbf{q}_2) , \tag{A9}$$

$$\begin{aligned}
G_3(\mathbf{q}_1, \mathbf{q}_2, \mathbf{q}_3, a) &= \frac{1}{6} \left[2O_{\beta\beta}(\mathbf{q}_1, \mathbf{q}_2, \mathbf{q}_3) + [2d_\gamma^{(2)} + d_{\gamma a}^{(3)} - 2(d_{\gamma a}^{(3)} + g(a))] O_{\beta\gamma}(\mathbf{q}_1, \mathbf{q}_2, \mathbf{q}_3) \right. \\
&+ \left(\frac{1}{4} d_{\gamma a}^{(3)} - \frac{1}{2} d_{\gamma b}^{(3)} \right) O_{\gamma\alpha_a}(\mathbf{q}_1, \mathbf{q}_2, \mathbf{q}_3) + \left(d_{\gamma b}^{(3)} - \frac{1}{2} d_{\gamma a}^{(3)} + 2g(a) \right) O_{\gamma\beta}(\mathbf{q}_1, \mathbf{q}_2, \mathbf{q}_3) \\
&\left. + \left(\frac{1}{2} d_{\gamma a}^{(3)} + d_{\gamma b}^{(3)} \right) O_{\gamma\gamma}(\mathbf{q}_1, \mathbf{q}_2, \mathbf{q}_3) + \text{cyclic} \right] ,
\end{aligned} \tag{A10}$$

³ With respect to this reference we have defined

$$d_\gamma = d_\gamma^{(2)} , \quad d_{\gamma\gamma} = \frac{1}{4} d_{\gamma a}^{(3)} + d_{\gamma b}^{(3)} , \quad d_{\gamma\alpha} = \frac{1}{4} d_{\gamma a}^{(3)} - \frac{1}{2} d_{\gamma b}^{(3)} .$$

where we have defined

$$\begin{aligned}
O_{\beta\beta}(\mathbf{q}_1, \mathbf{q}_2, \mathbf{q}_3) &\equiv \beta(\mathbf{q}_1, \mathbf{q}_2)\beta(\mathbf{q}_{12}, \mathbf{q}_3) , \\
O_{\beta\gamma}(\mathbf{q}_1, \mathbf{q}_2, \mathbf{q}_3) &\equiv \beta(\mathbf{q}_1, \mathbf{q}_2)\gamma(\mathbf{q}_{12}, \mathbf{q}_3) , \\
O_{\gamma\beta}(\mathbf{q}_1, \mathbf{q}_2, \mathbf{q}_3) &\equiv \gamma(\mathbf{q}_1, \mathbf{q}_2)\beta(\mathbf{q}_{12}, \mathbf{q}_3) , \\
O_{\gamma\gamma}(\mathbf{q}_1, \mathbf{q}_2, \mathbf{q}_3) &\equiv \gamma(\mathbf{q}_1, \mathbf{q}_2)\gamma(\mathbf{q}_{12}, \mathbf{q}_3) , \\
O_{\gamma\alpha_a}(\mathbf{q}_1, \mathbf{q}_2, \mathbf{q}_3) &\equiv \gamma(\mathbf{q}_1, \mathbf{q}_2)\alpha_a(\mathbf{q}_{12}, \mathbf{q}_3) ,
\end{aligned} \tag{A11}$$

and

$$\begin{aligned}
\alpha_a(\mathbf{q}_1, \mathbf{q}_2) &\equiv \alpha(\mathbf{q}_1, \mathbf{q}_2) - \alpha(\mathbf{q}_2, \mathbf{q}_1) , \\
g(a) &\equiv \int_0^a d \ln \tilde{a} f(\tilde{a}) \left[\frac{D(\tilde{a})}{D(a)} \right]^2 d_{\gamma}^{(2)}(\tilde{a}).
\end{aligned} \tag{A12}$$

In the EdS approximation, the time-dependent coefficients in the kernels above take the constant values

$$d_{\gamma, \text{EdS}}^{(2)} = \frac{6}{7} , \quad d_{\gamma a, \text{EdS}}^{(3)} = \frac{2}{7} , \quad d_{\gamma b, \text{EdS}}^{(3)} = \frac{5}{21}. \tag{A13}$$

The redshift space galaxy kernels are built as usual from the ones for density and velocity

$$Z_1(\mathbf{k}, a) = b_1 + f\mu_k^2 , \tag{A14}$$

$$Z_2(\mathbf{q}_1, \mathbf{q}_2, a) = K_2(\mathbf{q}_1, \mathbf{q}_2) + f\mu_k^2 G_2(\mathbf{q}_1, \mathbf{q}_2) + b_1 f\mu_k k \left(\frac{\mu_{q_1}}{q_1} + \frac{\mu_{q_2}}{q_2} \right) + f^2 \mu_k^2 k^2 \frac{\mu_{q_1} \mu_{q_2}}{q_1 q_2} , \tag{A15}$$

$$\begin{aligned}
Z_3(\mathbf{q}_1, \mathbf{q}_2, \mathbf{q}_3, a) &= K_3(\mathbf{q}_1, \mathbf{q}_2, a) + f\mu_k^2 G_3(\mathbf{q}_1, \mathbf{q}_2, \mathbf{q}_3) \\
&+ f\mu_k k \left[\frac{\mu_{q_1}}{q_1} K_2(\mathbf{q}_2, \mathbf{q}_3) + \frac{\mu_{q_{23}}}{q_{23}} G_2(\mathbf{q}_2, \mathbf{q}_3) \left(b_1 + f\mu_k k \frac{\mu_{q_1}}{q_1} \right) \right. \\
&+ \left. b_1 f\mu_k k \frac{\mu_{q_2} \mu_{q_3}}{q_2 q_3} + 2 \text{ cyclic} \right] \\
&+ f^3 \mu_k^3 k^3 \frac{\mu_{q_1} \mu_{q_2} \mu_{q_3}}{q_1 q_2 q_3}
\end{aligned} \tag{A16}$$

where we have used the notation $\mu_k \equiv \hat{\mathbf{k}} \cdot \hat{\mathbf{z}}$, $\mu_i \equiv \hat{\mathbf{q}}_i \cdot \hat{\mathbf{z}}$, $\mu_{ij} \equiv \hat{\mathbf{q}}_{ij} \cdot \hat{\mathbf{z}}$, and $\mathbf{q}_{12\dots n} \equiv \mathbf{q}_1 + \mathbf{q}_2 + \dots + \mathbf{q}_n$.

B. Galaxy Power Spectrum and Bispectrum in redshift space

The galaxy 1-loop power spectrum in redshift space is given by

$$\begin{aligned}
P_{g,s}^{1\text{-loop}}(k; a) &= Z_1(\mathbf{k}; a)^2 P_L(k; a) \\
&+ 2 \int \frac{d^3 \mathbf{q}}{(2\pi)^3} [Z_2(\mathbf{k} - \mathbf{q}, \mathbf{q}; a)^2] P_L(q; a) P_L(|\mathbf{k} - \mathbf{q}|; a) \\
&+ 6 Z_1(k; a) P_L(k; a) \int \frac{d^3 \mathbf{q}}{(2\pi)^3} Z_3(\mathbf{k}, \mathbf{q}, -\mathbf{q}; a) P_L(q; a) \\
&+ P_{ct}(\mathbf{k}; a) + P_{\epsilon}(\mathbf{k}; a)
\end{aligned} \tag{B1}$$

where $P_L(k; a)$ denotes the linear power spectrum, defined as

$$\langle \delta_{g,s}^{(1)}(\mathbf{k}, a) \delta_g^{(1)}(\mathbf{k}', a) \rangle = (2\pi)^3 \delta_D(\mathbf{k} + \mathbf{k}') P_L(k; a), \tag{B2}$$

and $P_{ct}(\mathbf{k}, a)$ and $P_\epsilon(\mathbf{k}, a)$ are respectively the counterterms and the stochastic terms, that account for the impact of small-scale physics on large scale modes. They are given by [42, 43]

$$P_{ct}(\mathbf{k}, a) = 2P_L(k)Z_1(\mathbf{k})\left(\frac{k}{k_M}\right)^2 (c_{ct} + c_{cr,1}\mu_k^2 + c_{cr,2}\mu_k^4), \quad (\text{B3})$$

$$P_\epsilon(\mathbf{k}, a) = \frac{1}{\bar{n}_g} \left(c_{\epsilon,0} + \left(\frac{k}{k_M}\right)^2 c_{\epsilon,1} + f\mu_k^2 \left(\frac{k}{k_M}\right)^2 c_{\epsilon,2} \right), \quad (\text{B4})$$

where the pivot scale k_M is of the order of the typical comoving scale of halos, \bar{n}_g is the mean number density of galaxies and we have used the notation $\mu_k \equiv \hat{\mathbf{k}} \cdot \hat{\mathbf{z}}$, being $\hat{\mathbf{z}}$ the line of sight.

The angle-averaged multipoles of the redshift-space power spectrum are defined as

$$P_\ell(k, z) = \frac{2\ell + 1}{2} \int_{-1}^1 d\mu_k P_g^{1\text{-loop}}(k, \mu_k; z) \mathcal{P}_\ell(\mu_k), \quad (\text{B5})$$

where $\mathcal{P}_\ell(\mu_k)$ are the Legendre polynomials of order ℓ . In this work we will consider the monopole ($\ell = 0$), the quadrupole ($\ell = 2$) and the hexadecapole ($\ell = 4$) of the galaxy power spectrum.

The tree-level bispectrum is given by

$$B(\mathbf{q}_1, \mathbf{q}_2, \mathbf{q}_3) = 2Z_1(\mathbf{q}_1)Z_1(\mathbf{q}_2)Z_2(\mathbf{q}_1, \mathbf{q}_2)P_L(q_1)P_L(q_2) + 2 \text{ perms.} \\ + B_\epsilon(\mathbf{q}_1, \mathbf{q}_2, \mathbf{q}_3), \quad (\text{B6})$$

where the shot noise contribution is [22, 42],

$$B_\epsilon(\mathbf{q}_1, \mathbf{q}_2, \mathbf{q}_3) = \frac{c_{\epsilon,3}}{\bar{n}_g^2} + \frac{1}{\bar{n}_g} \sum_{i=1}^3 (b_1 + f(\hat{\mathbf{q}}_i \cdot \hat{\mathbf{z}})^2) (c_{\epsilon,4} + c_{\epsilon,0}f(\hat{\mathbf{q}}_i \cdot \hat{\mathbf{z}})^2) P_L(q_i). \quad (\text{B7})$$

The bispectrum monopole and quadrupole are defined as

$$B_0(q_1, q_2, q_3) = \frac{1}{4\pi} \int_{-1}^1 d\mu_1 \int_0^{2\pi} d\phi B(q_1, q_2, q_3, \mu_1, \mu_2(\mu_1, \phi)), \quad (\text{B8})$$

$$B_2(q_1, q_2, q_3) = \frac{5}{4\pi} \int_{-1}^1 d\mu_1 \int_0^{2\pi} d\phi \mathcal{P}_2(\mu_3(\mu_1, \phi)) B(q_1, q_2, q_3, \mu_1, \mu_2(\mu_1, \phi)). \quad (\text{B9})$$

where we follow the conventions adopted in [22, 42], with

$$\mu_2 \equiv \mu_1 \hat{q}_1 \cdot \hat{q}_2 - \sqrt{1 - \mu_1^2} \sqrt{1 - (\hat{q}_1 \cdot \hat{q}_2)^2} \cos \phi, \quad (\text{B10})$$

$$\mu_3 \equiv -q_3^{-1} (q_1 \mu_1 + q_2 \mu_2(\mu_1, \phi)). \quad (\text{B11})$$

Further details on the implementation can be found in these references.

C. Impact of A_s Prior Choice

To assess how strongly our findings depend on fixing the amplitude parameter A_s to the true value used in the simulations, we repeat the analysis, this time imposing on A_s a 3σ Gaussian prior derived from *Planck* [39], following the approach of [40, 41]. Figure 7 shows the posterior distributions for both the single-box (Fig. 7a) and the full-volume (10 boxes, Fig. 7b) of the PT Challenge simulations.

As expected, changing the prior on A_s affects the parameter ε_f , owing to their degeneracy, discussed in Sect. III E. In the single-volume case, applying the *Planck* prior results in a slightly wider posterior for ε_f , but the corresponding shift in its central value remains well below 1σ . When considering the entire simulation volume, the *Planck* prior yields a broader posterior (still consistent at the 1σ level with that obtained for fixed A_s) and a larger shift in the central value of ε_f , which, however, still lies within 2σ of the true value.

For the parameter ε_{d_γ} , the posterior distributions remain unchanged when the priors on A_s are varied in either volume setup. This indicates that the parameter is only weakly affected by degeneracies, thereby reinforcing its robustness as a probe of departures from Λ CDM.

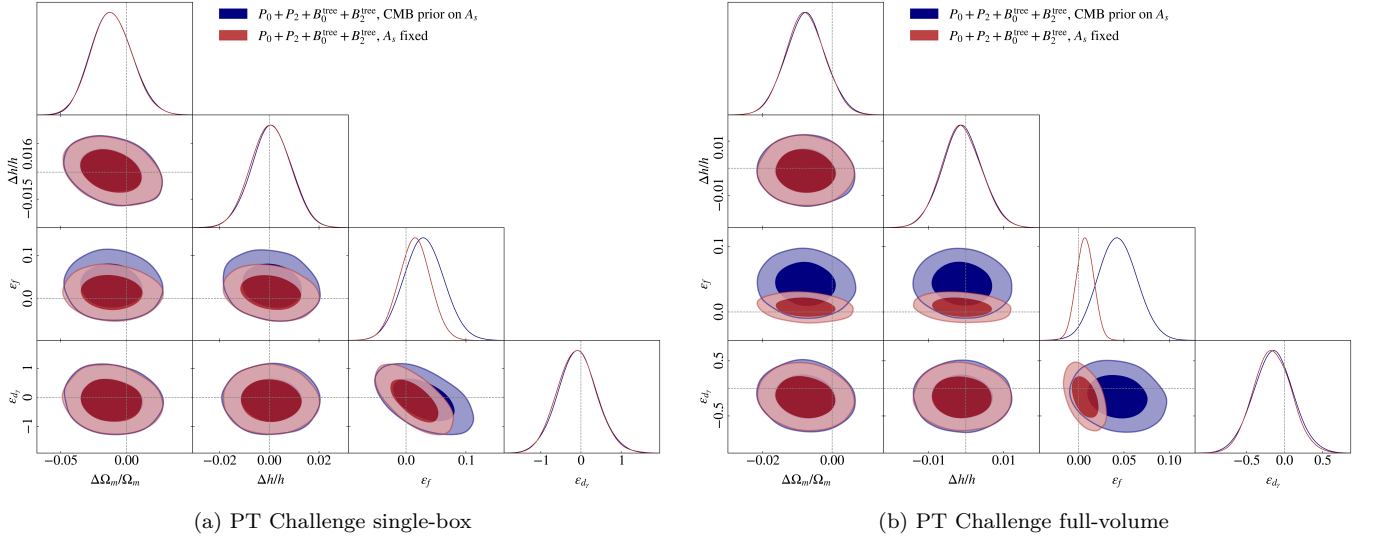


Figure 7: Posterior distributions for the PT Challenge simulations, comparing results obtained by fixing A_s to the true value of the simulations and by imposing a 3σ prior from *Planck*. On the left we show the results using the volume of a single simulation box, while on the right we consider the full volume covariance. We adopt $k_{\max, B_0} = 0.07 h \text{ Mpc}^{-1}$ and $k_{\max, B_2} = 0.04 h \text{ Mpc}^{-1}$. Dashed lines, centered at 0, represent the true values of the simulations.

D. Theoretical covariance

For the analysis of the PT Challenge simulations we employ a theoretical model for the covariance matrix of the power spectrum and the bispectrum, given the limited number of realizations. We briefly review here the derivation and the final formula adopted in the analysis.

The estimator for the redshift space power spectrum is defined as

$$\hat{P}_s(\mathbf{k}) = \frac{1}{VV_s} \int_{\mathbf{q} \in \mathbf{k}} d^3\mathbf{q} \delta_s(\mathbf{q}) \delta_s(-\mathbf{q}), \quad (\text{D1})$$

where the shell volume V_s is defined such that eq. D1 is an unbiased estimator in the thin-shell approximation, $V_s \simeq 4\pi k^2 \delta k$. The estimator for the power spectrum ℓ -multipole is then given by

$$\hat{P}_\ell(k) = \frac{2\ell + 1}{2} \int_{-1}^1 d\mu \mathcal{L}_\ell(\mu) \hat{P}_s(\mathbf{k}). \quad (\text{D2})$$

One can easily estimate the gaussian covariance for such estimator, obtaining

$$\text{Cov}(P_\ell, P_{\ell'}) (k, k') = (2\pi)^3 \frac{(2\ell + 1)(2\ell' + 1)}{2VV_s} \delta_{k, k'}^K \int_{-1}^1 d\mu \mathcal{L}_\ell(\mu) \mathcal{L}_{\ell'}(\mu) P_s^2(\mathbf{k}), \quad (\text{D3})$$

where δ^K indicates a Kronecker delta. Notice that the redshift space power spectrum $P_s(\mathbf{k})$ in this expression is the linear one, including the constant shot-noise term

$$P_s(\mathbf{k}) = (b_1 + f\mu^2)^2 P_L(k) + \frac{1}{n}. \quad (\text{D4})$$

For the bispectrum, we consider the following unbiased estimators for the redshift space multipoles [57]

$$\hat{B}_\ell(k_1, k_2, k_3) = \frac{(2\ell + 1)}{VV_{123}} \int_{\mathbf{q}_1 \in k_1} d^3\mathbf{q}_1 \int_{\mathbf{q}_2 \in k_2} d^3\mathbf{q}_2 \int_{\mathbf{q}_3 \in k_3} d^3\mathbf{q}_3 \delta_D(\mathbf{q}_{123}) \delta_s(\mathbf{q}_1) \delta_s(\mathbf{q}_2) \delta_s(\mathbf{q}_3) \mathcal{L}_\ell(\mu_1), \quad (\text{D5})$$

where the integrals over \mathbf{q}_i 's are performed over the shell width $[k_i - \Delta k/2, k_i + \Delta k/2]$, $\mu_1 = \hat{\mathbf{q}}_1 \cdot \hat{\mathbf{n}}$ and V_{123} is the triangular bin volume given by

$$V_{123} = \int_{k_1} d^3 \mathbf{q}_1 \int_{k_1} d^3 \mathbf{q}_2 \int_{k_1} d^3 \mathbf{q}_3 \delta_D(\mathbf{q}_{123}) \simeq 8\pi^2 k_1 k_2 k_3 \Delta k^3. \quad (\text{D6})$$

Given this estimator, we can compute the covariance among two different triangles T and T' as

$$\text{Cov}(T, T') = \langle \hat{B}_\ell(k_1, k_2, k_3) \hat{B}_{\ell'}(k'_1, k'_2, k'_3) \rangle - \langle \hat{B}_\ell(k_1, k_2, k_3) \rangle \langle \hat{B}_{\ell'}(k'_1, k'_2, k'_3) \rangle, \quad (\text{D7})$$

which eventually results in

$$\text{Cov}(T, T') = \text{Cov}(T, T')^{PPP} + \text{Cov}(T, T')^{BB} + \text{Cov}(T, T')^{PT} + \text{Cov}(T, T')^{6pt}. \quad (\text{D8})$$

The ‘ PPP ’ term denotes the ‘gaussian’ contribution, expressed as the product of three power spectra. The ‘ BB ’ term corresponds to the contribution involving the product of two bispectra, ‘ PT ’ includes the product of a power spectrum and a trispectrum, and ‘ $6pt$ ’ represents the contribution arising from the connected six-point function. We will only include the gaussian term, as the others have been shown to give negligible contributions in the range of scales considered in our analysis [58, 59]. Moreover, for the same reason, in the PT challenge we neglect the contribution to the covariance arising from the cross-correlation between the power spectrum and the bispectrum, as the analysis is restricted to large scales where this term is negligible. For the analysis of BOSS data, we will make use of the numerical covariance matrix estimated from 2048 Patchy mocks [34]. It is given by

$$\begin{aligned} \text{Cov}(T, T')^{PPP} = & \frac{(2\ell + 1)(2\ell' + 1)}{V^2 V_{123}^2} \int_{\mathbf{q}_1} \int_{\mathbf{q}_2} \int_{\mathbf{q}_3} \int_{\mathbf{q}'_1} \int_{\mathbf{q}'_2} \int_{\mathbf{q}'_3} \delta_D(\mathbf{q}_{123}) \delta_D(\mathbf{q}'_{123}) \mathcal{L}_\ell(\mu_1) \mathcal{L}_{\ell'}(\mu'_1) \times \\ & \times \left(\langle \delta_s(\mathbf{q}_1) \delta_s(\mathbf{q}'_1) \rangle \langle \delta_s(\mathbf{q}_2) \delta_s(\mathbf{q}'_2) \rangle \langle \delta_s(\mathbf{q}_3) \delta_s(\mathbf{q}'_3) \rangle + 5 \text{ perms.} \right). \end{aligned} \quad (\text{D9})$$

We first integrate over \mathbf{q}'_1 , \mathbf{q}'_2 and \mathbf{q}'_3 , and exploit the definition $V = (2\pi)^3 \delta_D(0)$ to simplify the expression

$$\begin{aligned} \text{Cov}(T, T')^{PPP} = & (2\pi)^6 \frac{(2\ell + 1)(2\ell' + 1)}{V V_{123}^2} \int_{\mathbf{q}_1} \int_{\mathbf{q}_2} \int_{\mathbf{q}_3} \delta_D(\mathbf{q}_{123}) \left[c_1 \mathcal{L}_\ell(\mu_1) \mathcal{L}_{\ell'}(-\mu_1) + c_2 \mathcal{L}_\ell(\mu_1) \mathcal{L}_{\ell'}(-\mu_2) + c_3 \mathcal{L}_\ell(\mu_1) \mathcal{L}_{\ell'}(-\mu_3) \right] \\ & \times P_s(\mathbf{q}_1) P_s(\mathbf{q}_2) P_s(\mathbf{q}_3). \end{aligned} \quad (\text{D10})$$

To further simplify the expression for the bispectrum covariance, we expand the power spectra in multipoles using

$$P_s(\mathbf{k}) = \sum_{\ell} \mathcal{L}_\ell(\mu) P_\ell(k), \quad (\text{D11})$$

such that

$$\begin{aligned} \text{Cov}(T, T')^{PPP} = & (2\pi)^6 \frac{(2\ell + 1)(2\ell' + 1)}{V V_{123}^2} \int_{\mathbf{q}_1} \int_{\mathbf{q}_2} \int_{\mathbf{q}_3} \delta_D(\mathbf{q}_{123}) \left[c_1 \mathcal{L}_\ell(\mu_1) \mathcal{L}_{\ell'}(-\mu_1) + c_2 \mathcal{L}_\ell(\mu_1) \mathcal{L}_{\ell'}(-\mu_2) + c_3 \mathcal{L}_\ell(\mu_1) \mathcal{L}_{\ell'}(-\mu_3) \right] \\ & \times \mathcal{L}_{\ell_1}(\mu_1) \mathcal{L}_{\ell_2}(\mu_2) \mathcal{L}_{\ell_3}(\mu_3) \sum_{\ell_1, \ell_2, \ell_3} P_{\ell_1}(q_1) P_{\ell_2}(q_2) P_{\ell_3}(q_3), \end{aligned} \quad (\text{D12})$$

which can be rewritten in the compact form (assuming thin-enough bins)

$$\text{Cov}(T, T')^{PPP} = (2\pi)^6 \frac{(2\ell + 1)(2\ell' + 1)}{V V_{123}} \sum_{\ell_1, \ell_2, \ell_3} F_{\ell_1 \ell_2 \ell_3}^{\ell \ell'}(k_1, k_2, k_3) P_{\ell_1}(k_1) P_{\ell_2}(k_2) P_{\ell_3}(k_3), \quad (\text{D13})$$

with

$$F_{\ell_1 \ell_2 \ell_3}^{\ell \ell'}(k_1, k_2, k_3) = \frac{1}{4\pi} \int_0^{2\pi} d\xi \int_{-1}^1 d\mu_1 \left[c_1 \mathcal{L}_\ell(\mu_1) \mathcal{L}_{\ell'}(-\mu_1) + c_2 \mathcal{L}_\ell(\mu_1) \mathcal{L}_{\ell'}(-\mu_2) + c_3 \mathcal{L}_\ell(\mu_1) \mathcal{L}_{\ell'}(-\mu_3) \right] \mathcal{L}_{\ell_1}(\mu_1) \mathcal{L}_{\ell_2}(\mu_2) \mathcal{L}_{\ell_3}(\mu_3). \quad (\text{D14})$$

The coefficients c_1 , c_2 and c_3 are symmetry coefficients such that

$$\begin{aligned}
 \{c_1, c_2, c_3\} &= \{2, 2, 2\} & \text{if } k_1 = k_2 = k_3, \\
 \{c_1, c_2, c_3\} &= \{2, 0, 0\} & \text{if } k_2 = k_3, \\
 \{c_1, c_2, c_3\} &= \{1, 1, 0\} & \text{if } k_1 = k_2, \\
 \{c_1, c_2, c_3\} &= \{1, 0, 0\} & \text{if } k_1 \neq k_2 \neq k_3.
 \end{aligned}
 \tag{D15}$$

Equation (D13), already found in [36], is the expression we will use to compute the covariance of the bispectrum multipoles. The number density and volume inserted in these expressions are the ones of the PT challenge, reported in section III B. For the bias parameters we adopt the ones estimated in appendix E.

E. Complete parameter space constraints

For completeness, we display the full triangle plots obtained fitting BOSS and PT Challenge power spectrum and bispectrum multipoles, respectively in Fig. 8 and Fig. 9. The posterior means with 68% confidence intervals are reported in Tab. IV and Tab. V.

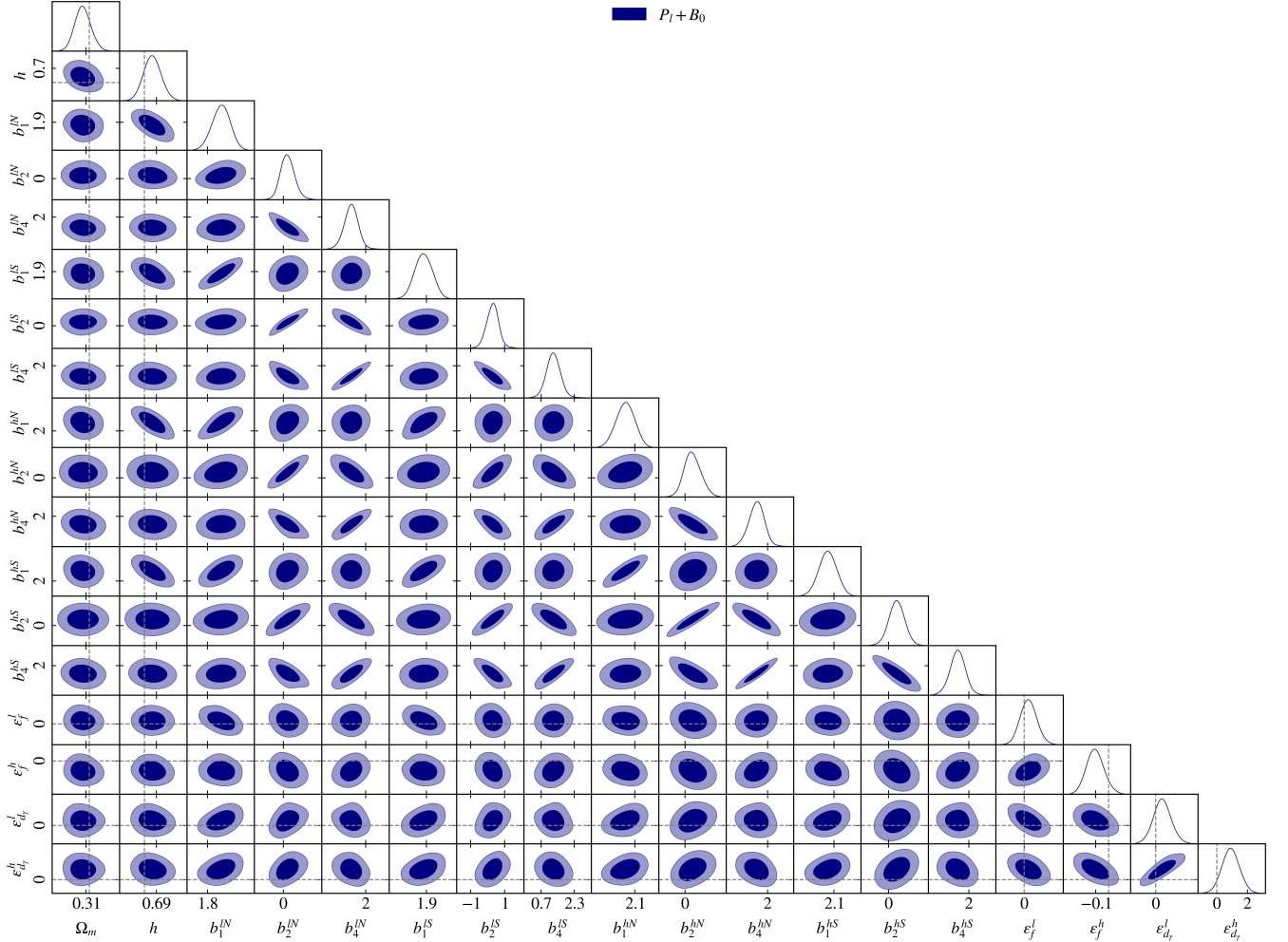


Figure 8: Full posterior distributions from the analysis of BOSS power spectrum multipoles P_l and bispectrum monopole B_0 , with n_s and A_s fixed to the *Planck* [39] best-fits. Dashed lines represent the *Planck* best-fit values.

Dataset	b_1	b_2	b_4
LOWZ NGC	1.877 ± 0.051	$0.25^{+0.38}_{-0.43}$	1.32 ± 0.34
LOWZ SGC	1.884 ± 0.052	0.29 ± 0.38	1.30 ± 0.34
CMASS NGC	2.055 ± 0.045	$0.45^{+0.45}_{-0.53}$	1.46 ± 0.38
CMASS SGC	2.069 ± 0.045	0.50 ± 0.42	1.44 ± 0.38

Table IV: Constraints on bias parameters b_1 , b_2 and b_4 from the BOSS LOWZ and CMASS Northern and Southern galactic caps (NGC and SGC) datasets, with n_s and A_s fixed to *Planck* [39] best-fits. Reported values correspond to posterior means with 68% confidence intervals.

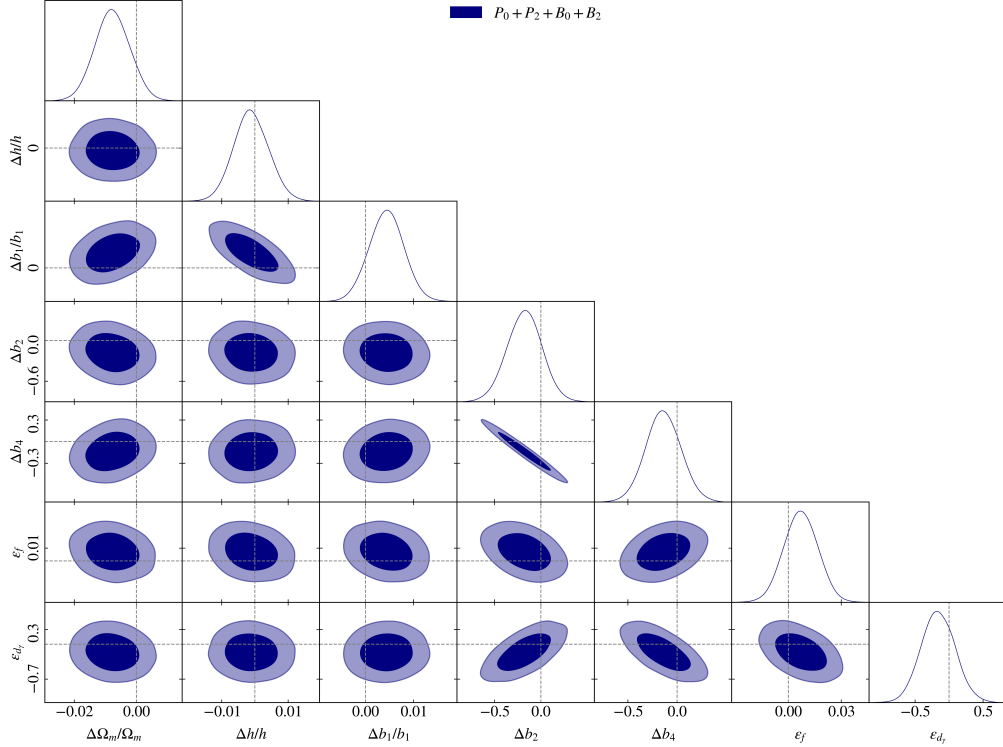


Figure 9: Full posterior distributions for the joint analysis of power spectrum and bispectrum multipoles of the PT Challenge simulations, with n_s and A_s fixed to the true values of the simulations. We adopt $k_{\max, B_0} = 0.07h \text{ Mpc}^{-1}$ and $k_{\max, B_2} = 0.04h \text{ Mpc}^{-1}$. Dashed lines represent the true values of the simulations for the cosmological and bootstrap parameters, and the inferred values for the bias ones (see Appendix E).

Dataset	$\Delta b_1/b_1$	Δb_2	Δb_4
$P_0 + P_2 + B_0 + B_2$	0.0044 ± 0.0037	-0.18 ± 0.19	-0.14 ± 0.18

Table V: Constraints on bias parameters b_1 , b_2 and b_4 from the PT Challenge simulations, with n_s and A_s fixed to the true values. Reported values correspond to posterior means with 68% confidence intervals. Here, $\Delta b_i = b_i - \bar{b}_i$ denotes the deviation of bias parameter b_i from its value inferred as discussed in Appendix E.

The estimated true values for the bias parameters reported in Table V were obtained using the peak-background split (PBS) approach [30], see also [60, 61]. In this framework, (local) halo biases are interpreted as the response of the halo abundance to long-wavelength density perturbations. To compute such response, the key ingredient is the halo mass function, which describes the number distribution of halos given a specific halo mass. On top of that, the second key ingredient is the halo occupation distribution (HOD): this describes how galaxies populate halos of different masses. The procedure to estimate the halo mass function and the HOD for the PT Challenge simulations is described in [28], and we adopted their function to estimate the bias parameters. Given these two ingredients, one can estimate

the bias parameters as

$$b_{\mathcal{O}}(z) = \frac{\int dM \frac{dn_h}{dM}(M, z) N_g(M, z) b_{\mathcal{O}}(M, z)}{\int dM \frac{dn_h}{dM}(M, z) N_g(M, z)}, \quad (\text{E1})$$

where $dn_h(M, z)/dM$ is the halo mass function, $N_g(M, z)$ is HOD function. The mass dependent biases $b_{\mathcal{O}}(M, z)$ can be obtained assuming universality of the halo mass function. One of the best empirical functions for the linear bias b_1 is [62]

$$b_1(M) = 1 - A \frac{\nu(M)^a}{\nu(M)^a + \delta_c^a} + B\nu(M)^b + C\nu(M)^c \quad (\text{E2})$$

with $\delta_c = 1.686$ being the critical overdensity for spherical collapse, ν is the peak height defined as

$$\nu(M) = \frac{\delta_c}{\sigma(M)}, \quad (\text{E3})$$

with $\sigma(M)$ defined as the linear matter variance defined on the Lagrangian scale of the halo $R = (3M/4\pi\bar{\rho}_m)^{1/3}$ filtered with a top-hat window function

$$\sigma^2(M, z) \equiv \int d^3\mathbf{q} P_{\text{lin}}(k, z) W^2(k, R(M)). \quad (\text{E4})$$

The parameters in eq. E2 are obtained by fitting to different simulations

$$\begin{aligned} A &= 1.0 + 0.24 y e^{-(4/y)^4}, & a &= 0.44y - 0.88, \\ B &= 0.183, & b &= 1.5, \\ C &= 0.019 + 0.107 y + 0.19 e^{-(4/y)^4}, & c &= 2.4, \end{aligned}$$

where $y = \log 200$. Following the notation of [63], we can write the galaxy density perturbation field at second perturbative order as

$$\delta_g^{(2)}(\mathbf{x}) = b_1 \delta^{(2)}(\mathbf{x}) + \frac{b_{\delta^2}}{2} [\delta^{(1)2} - \langle \delta^{(1)2} \rangle] + b_{K^2} [K^2(\mathbf{x}) - \langle K^2 \rangle], \quad (\text{E5})$$

where the tidal operator is defined as

$$K_{ij}(\mathbf{x}) = \left[\frac{\partial_i \partial_j}{\nabla^2} - \frac{1}{3} \delta_{ij}^K \right] \delta(\mathbf{x}). \quad (\text{E6})$$

The PBS approach cannot predict non-local bias parameters, for which more empirical relations were found: we will make use of the relation between the linear second order bias b_{δ^2} and b_1 found in [64]

$$b_{\delta^2}(M) = 0.412 - 2.143 b_1(M) + 0.929 b_1^2(M) + 0.008 b_1^3(M). \quad (\text{E7})$$

PBS does not provide for an analytical expression for the non-local bias parameters [30]. One can see that the local Lagrangian approximation (Lagrangian local-in-matter-density, LLIMD) constrains the shape of the tidal bias to be

$$b_{K^2}^{\text{LLIMD}}(M) = -\frac{2}{7} (b_1(M) - 1), \quad (\text{E8})$$

which has been shown to be a poor fit to actual data, see [63, 65–67]. Methods based on the excursion-set approach predict a slightly modified version of the LLIMD relation, yielding [68]

$$b_{K^2}^{\text{Ex.set}}(M) = 0.524 - 0.547 b_1(M) + 0.046 b_1^2(M), \quad (\text{E9})$$

which seems to agree better with data from simulations [65]. Here we will adopt a refined version of this relation based on the findings of [66]

$$b_{K^2}(M) = 0.932 - 1.297 b_1(M) + 0.345 b_1^2(M) - 0.034 b_1^3(M). \quad (\text{E10})$$

After inserting eqs. E7 and E10 into eq. E1 one can easily calculate the expected values for the bias parameters $b_1(z)$, $b_{\delta^2}(z)$ and $b_{K^2}(z)$ at a given redshift z and compare with the best-fit results. Let us stress that the second order biases shown in eqs. E7 and E10 are equivalent to the bias parameters adopted in this work. The mapping between the two bases is explicitly given by

$$b_2(z) = \frac{7}{2}b_{K^2}(z) + b_1(z), \quad b_4(z) = \frac{1}{2}b_{\delta^2}(z) - \frac{17}{6}b_{K^2}(z). \quad (\text{E11})$$

The values computed with this procedure are compared with those obtained by fitting to the PT Challenge data, and the comparison is shown in figures 9 and table V, which results in a good agreement.

-
- [1] Y. Mellier *et al.* (Euclid), Euclid. I. Overview of the Euclid mission, *Astron. Astrophys.* **697**, A1 (2025), [arXiv:2405.13491 \[astro-ph.CO\]](#).
 - [2] A. Aghamousa *et al.* (DESI), The DESI Experiment Part I: Science, Targeting, and Survey Design (2016), [arXiv:1611.00036 \[astro-ph.IM\]](#).
 - [3] A. G. Adame *et al.* (DESI), DESI 2024 VI: cosmological constraints from the measurements of baryon acoustic oscillations, *JCAP* **02**, 021, [arXiv:2404.03002 \[astro-ph.CO\]](#).
 - [4] A. G. Adame *et al.* (DESI), DESI 2024 V: Full-Shape galaxy clustering from galaxies and quasars, *JCAP* **09**, 008, [Erratum: *JCAP* **02**, E02 (2026)], [arXiv:2411.12021 \[astro-ph.CO\]](#).
 - [5] M. Abdul Karim *et al.* (DESI), DESI DR2 results. II. Measurements of baryon acoustic oscillations and cosmological constraints, *Phys. Rev. D* **112**, 083515 (2025), [arXiv:2503.14738 \[astro-ph.CO\]](#).
 - [6] K. Lodha *et al.* (DESI), Extended dark energy analysis using DESI DR2 BAO measurements, *Phys. Rev. D* **112**, 083511 (2025), [arXiv:2503.14743 \[astro-ph.CO\]](#).
 - [7] G. D’Amico, M. Marinucci, M. Pietroni, and F. Vernizzi, The large scale structure bootstrap: perturbation theory and bias expansion from symmetries, *JCAP* **10**, 069, [arXiv:2109.09573 \[astro-ph.CO\]](#).
 - [8] M. Marinucci, K. Pardede, and M. Pietroni, Bootstrapping Lagrangian perturbation theory for the large scale structure, *JCAP* **10**, 051, [arXiv:2405.08413 \[astro-ph.CO\]](#).
 - [9] M. Peron, T. Nishimichi, M. Pietroni, and A. Taruya, Renormalized perturbation theory at field-level: the LSS bootstrap in GridSPT, *JCAP* **10**, 098, [arXiv:2506.07105 \[astro-ph.CO\]](#).
 - [10] T. Fujita and Z. Vlah, Perturbative description of biased tracers using consistency relations of LSS, *JCAP* **10**, 059, [arXiv:2003.10114 \[astro-ph.CO\]](#).
 - [11] A. Ansari, A. Banerjee, S. Jain, and S. Lalsodagar, Bootstrapping LSS perturbation theory beyond third order (2025), [arXiv:2504.01078 \[astro-ph.CO\]](#).
 - [12] L. Amendola, M. Marinucci, M. Pietroni, and M. Quartin, Improving precision and accuracy in cosmology with model-independent spectrum and bispectrum, *JCAP* **01**, 001, [arXiv:2307.02117 \[astro-ph.CO\]](#).
 - [13] L. Amendola, M. Pietroni, and M. Quartin, Fisher matrix for the one-loop galaxy power spectrum: measuring expansion and growth rates without assuming a cosmological model, *JCAP* **11**, 023, [arXiv:2205.00569 \[astro-ph.CO\]](#).
 - [14] D. Baumann, A. Nicolis, L. Senatore, and M. Zaldarriaga, Cosmological Non-Linearities as an Effective Fluid, *JCAP* **07**, 051, [arXiv:1004.2488 \[astro-ph.CO\]](#).
 - [15] J. J. M. Carrasco, M. P. Hertzberg, and L. Senatore, The Effective Field Theory of Cosmological Large Scale Structures, *JHEP* **09**, 082, [arXiv:1206.2926 \[astro-ph.CO\]](#).
 - [16] A. Perko, L. Senatore, E. Jennings, and R. H. Wechsler, Biased tracers in redshift space in the eft of large-scale structure (2016), [arXiv:1610.09321 \[astro-ph.CO\]](#).
 - [17] G. D’Amico, L. Senatore, and P. Zhang, Limits on w CDM from the EFTofLSS with the PyBird code, *JCAP* **01**, 006, [arXiv:2003.07956 \[astro-ph.CO\]](#).
 - [18] O. H. E. Philcox, M. M. Ivanov, G. Cabass, M. Simonović, M. Zaldarriaga, and T. Nishimichi, Cosmology with the redshift-space galaxy bispectrum monopole at one-loop order, *Phys. Rev. D* **106**, 043530 (2022), [arXiv:2206.02800 \[astro-ph.CO\]](#).
 - [19] M. M. Ivanov, O. H. E. Philcox, G. Cabass, T. Nishimichi, M. Simonović, and M. Zaldarriaga, Cosmology with the galaxy bispectrum multipoles: Optimal estimation and application to BOSS data, *Phys. Rev. D* **107**, 083515 (2023), [arXiv:2302.04414 \[astro-ph.CO\]](#).
 - [20] T. Bakx, M. M. Ivanov, O. H. E. Philcox, and Z. Vlah, One-Loop Galaxy Bispectrum: Consistent Theory, Efficient Analysis with COBRA, and Implications for Cosmological Parameters (2025), [arXiv:2507.22110 \[astro-ph.CO\]](#).
 - [21] M. M. Ivanov, O. H. E. Philcox, T. Nishimichi, M. Simonović, M. Takada, and M. Zaldarriaga, Precision analysis of the redshift-space galaxy bispectrum, *Phys. Rev. D* **105**, 063512 (2022), [arXiv:2110.10161 \[astro-ph.CO\]](#).
 - [22] G. D’Amico, Y. Donath, M. Lewandowski, L. Senatore, and P. Zhang, The BOSS bispectrum analysis at one loop from the Effective Field Theory of Large-Scale Structure, *JCAP* **05**, 059, [arXiv:2206.08327 \[astro-ph.CO\]](#).
 - [23] A. Chudaykin, M. M. Ivanov, and O. H. E. Philcox, Reanalyzing DESI DR1. I. Λ CDM constraints from the power spectrum and bispectrum, *Phys. Rev. D* **113**, 063502 (2026), [arXiv:2507.13433 \[astro-ph.CO\]](#).
 - [24] A. Chudaykin, M. M. Ivanov, and O. H. E. Philcox, Reanalyzing DESI DR1: 2. Constraints on Dark Energy, Spatial Curvature, and Neutrino Masses (2025), [arXiv:2511.20757 \[astro-ph.CO\]](#).

- [25] A. Chudaykin, M. M. Ivanov, and O. H. E. Philcox, Reanalyzing DESI DR1: 3. Constraints on Inflation from Galaxy Power Spectra & Bispectra (2025), [arXiv:2512.04266 \[astro-ph.CO\]](#).
- [26] A. Chudaykin, M. M. Ivanov, and O. H. E. Philcox, Reanalyzing DESI DR1: 5. Cosmological Constraints with Simulation-Based Priors (2026), [arXiv:2602.18554 \[astro-ph.CO\]](#).
- [27] B. Reid, S. Ho, N. Padmanabhan, W. J. Percival, J. Tinker, R. Tojeiro, M. White, D. J. Eisenstein, C. Maraston, A. J. Ross, A. G. Sanchez, D. Schlegel, E. Sheldon, M. A. Strauss, D. Thomas, D. Wake, F. Beutler, D. Bizyaev, A. S. Bolton, J. R. Brownstein, C.-H. Chuang, K. Dawson, P. Harding, F.-S. Kitaura, A. Leauthaud, K. Masters, C. K. McBride, S. More, M. D. Olmstead, D. Oravetz, S. E. Nuza, K. Pan, J. Parejko, J. Pforr, F. Prada, S. Rodriguez-Torres, S. Salazar-Albornoz, L. Samushia, D. P. Schneider, C. G. Scoccola, A. Simmons, and M. Vargas-Magana, *Sdss-iii baryon oscillation spectroscopic survey data release 12: galaxy target selection and large scale structure catalogues* (2015), [arXiv:1509.06529 \[astro-ph.CO\]](#).
- [28] T. Nishimichi, G. D’Amico, M. M. Ivanov, L. Senatore, M. Simonović, M. Takada, M. Zaldarriaga, and P. Zhang, Blinded challenge for precision cosmology with large-scale structure: results from effective field theory for the redshift-space galaxy power spectrum, *Phys. Rev. D* **102**, 123541 (2020), [arXiv:2003.08277 \[astro-ph.CO\]](#).
- [29] F. Bernardreau, S. Colombi, E. Gaztanaga, and R. Scoccimarro, Large scale structure of the universe and cosmological perturbation theory, *Phys. Rept.* **367**, 1 (2002), [arXiv:astro-ph/0112551](#).
- [30] V. Desjacques, D. Jeong, and F. Schmidt, Large-Scale Galaxy Bias, *Phys. Rept.* **733**, 1 (2018), [arXiv:1611.09787 \[astro-ph.CO\]](#).
- [31] O. H. E. Philcox and M. M. Ivanov, BOSS DR12 full-shape cosmology: Λ CDM constraints from the large-scale galaxy power spectrum and bispectrum monopole, *Phys. Rev. D* **105**, 043517 (2022), [arXiv:2112.04515 \[astro-ph.CO\]](#).
- [32] C. Alcock and B. Paczynski, An evolution free test for non-zero cosmological constant, *Nature* **281**, 358 (1979).
- [33] S. Alam, M. Ata, S. Bailey, F. Beutler, D. Bizyaev, J. A. Blazek, A. S. Bolton, J. R. Brownstein, A. Burden, C.-H. Chuang, J. Comparat, A. J. Cuesta, K. S. Dawson, D. J. Eisenstein, S. Escoffier, H. Gil-Marín, J. N. Grieb, N. Hand, S. Ho, K. Kinemuchi, D. Kirkby, F. Kitaura, E. Malanushenko, V. Malanushenko, C. Maraston, C. K. McBride, R. C. Nichol, M. D. Olmstead, D. Oravetz, N. Padmanabhan, N. Palanque-Delabrouille, K. Pan, M. Pellejero-Ibanez, W. J. Percival, P. Petitjean, F. Prada, A. M. Price-Whelan, B. A. Reid, S. A. Rodríguez-Torres, N. A. Roe, A. J. Ross, N. P. Ross, G. Rossi, J. A. Rubiño-Martín, S. Saito, S. Salazar-Albornoz, L. Samushia, A. G. Sánchez, S. Satpathy, D. J. Schlegel, D. P. Schneider, C. G. Scóccola, H.-J. Seo, E. S. Sheldon, A. Simmons, A. Slosar, M. A. Strauss, M. E. C. Swanson, D. Thomas, J. L. Tinker, R. Tojeiro, M. V. Magaña, J. A. Vazquez, L. Verde, D. A. Wake, Y. Wang, D. H. Weinberg, M. White, W. M. Wood-Vasey, C. Yèche, I. Zehavi, Z. Zhai, and G.-B. Zhao, The clustering of galaxies in the completed sdss-iii baryon oscillation spectroscopic survey: cosmological analysis of the dr12 galaxy sample, *Monthly Notices of the Royal Astronomical Society* **470**, 2617–2652 (2017).
- [34] F.-S. Kitaura, S. Rodríguez-Torres, C.-H. Chuang, C. Zhao, F. Prada, H. Gil-Marín, H. Guo, G. Yepes, A. Klypin, C. G. Scóccola, J. Tinker, C. McBride, B. Reid, A. G. Sánchez, S. Salazar-Albornoz, J. N. Grieb, M. Vargas-Magana, A. J. Cuesta, M. Neyrinck, F. Beutler, J. Comparat, W. J. Percival, and A. Ross, The clustering of galaxies in the sdss-iii baryon oscillation spectroscopic survey: mock galaxy catalogues for the boss final data release, *Monthly Notices of the Royal Astronomical Society* **456**, 4156–4173 (2016).
- [35] D. Wadekar, M. M. Ivanov, and R. Scoccimarro, Cosmological constraints from BOSS with analytic covariance matrices, *Phys. Rev. D* **102**, 123521 (2020), [arXiv:2009.00622 \[astro-ph.CO\]](#).
- [36] F. Rizzo, C. Moretti, K. Pardede, A. Eggemeier, A. Oddo, E. Sefusatti, C. Porciani, and P. Monaco, The halo bispectrum multipoles in redshift space, *JCAP* **01**, 031, [arXiv:2204.13628 \[astro-ph.CO\]](#).
- [37] T. Brinckmann and J. Lesgourgues, *Montepython 3: boosted mcmc sampler and other features* (2018), [arXiv:1804.07261 \[astro-ph.CO\]](#).
- [38] B. Audren, J. Lesgourgues, K. Benabed, and S. Prunet, Conservative Constraints on Early Cosmology: an illustration of the Monte Python cosmological parameter inference code, *JCAP* **1302**, 001, [arXiv:1210.7183 \[astro-ph.CO\]](#).
- [39] N. Aghanim *et al.* (Planck), Planck 2018 results. VI. Cosmological parameters, *Astron. Astrophys.* **641**, A6 (2020), [Erratum: *Astron. Astrophys.* 652, C4 (2021)], [arXiv:1807.06209 \[astro-ph.CO\]](#).
- [40] M. Tsedrik, C. Moretti, P. Carrilho, F. Rizzo, and A. Pourtsidou, Interacting dark energy from the joint analysis of the power spectrum and bispectrum multipoles with the EFTofLSS, *Mon. Not. Roy. Astron. Soc.* **520**, 2611 (2023), [arXiv:2207.13011 \[astro-ph.CO\]](#).
- [41] P. Carrilho, C. Moretti, and A. Pourtsidou, Cosmology with the EFTofLSS and BOSS: dark energy constraints and a note on priors, *JCAP* **01**, 028, [arXiv:2207.14784 \[astro-ph.CO\]](#).
- [42] G. D’Amico, Y. Donath, M. Lewandowski, L. Senatore, and P. Zhang, The one-loop bispectrum of galaxies in redshift space from the Effective Field Theory of Large-Scale Structure, *JCAP* **07**, 041, [arXiv:2211.17130 \[astro-ph.CO\]](#).
- [43] G. D’Amico, M. Lewandowski, L. Senatore, and P. Zhang, Limits on primordial non-Gaussianities from BOSS galaxy-clustering data, *Phys. Rev. D* **111**, 063514 (2025), [arXiv:2201.11518 \[astro-ph.CO\]](#).
- [44] L. Piga, M. Marinucci, G. D’Amico, M. Pietroni, F. Vernizzi, and B. S. Wright, Constraints on modified gravity from the BOSS galaxy survey, *JCAP* **04**, 038, [arXiv:2211.12523 \[astro-ph.CO\]](#).
- [45] A. Gelman and D. B. Rubin, Inference from Iterative Simulation Using Multiple Sequences, *Statist. Sci.* **7**, 457 (1992).
- [46] A. Lewis, Getdist: a python package for analysing monte carlo samples, *Journal of Cosmology and Astroparticle Physics* **2025** (08), 025.
- [47] G. D’Amico, J. Gleyzes, N. Kokron, K. Markovic, L. Senatore, P. Zhang, F. Beutler, and H. Gil-Marín, The Cosmological Analysis of the SDSS/BOSS data from the Effective Field Theory of Large-Scale Structure, *JCAP* **05**, 005, [arXiv:1909.05271 \[astro-ph.CO\]](#).
- [48] V. Desjacques, D. Jeong, and F. Schmidt, The Galaxy Power Spectrum and Bispectrum in Redshift Space, *JCAP* **12**, 035,

- arXiv:1806.04015 [astro-ph.CO].
- [49] T. Simon, P. Zhang, V. Poulin, and T. L. Smith, Consistency of effective field theory analyses of the BOSS power spectrum, *Phys. Rev. D* **107**, 123530 (2023), arXiv:2208.05929 [astro-ph.CO].
 - [50] P. Taule, M. Marinucci, G. Biselli, M. Pietroni, and F. Vernizzi, Constraints on dark energy and modified gravity from the BOSS Full-Shape and DESI BAO data, *JCAP* **03**, 036, arXiv:2409.08971 [astro-ph.CO].
 - [51] E. Krause *et al.* (Beyond-2pt), A Parameter-Masked Mock Data Challenge for Beyond-Two-Point Galaxy Clustering Statistics, *Astrophys. J.* **990**, 99 (2025), arXiv:2405.02252 [astro-ph.CO].
 - [52] M. Peron, G. Jung, M. Liguori, and M. Pietroni, Constraining primordial non-Gaussianity from large scale structure with the wavelet scattering transform, *JCAP* **07**, 021, arXiv:2403.17657 [astro-ph.CO].
 - [53] M. Marinucci *et al.*, The constraining power of the marked power spectrum: an analytical study, *JCAP* **09**, 036, arXiv:2411.14377 [astro-ph.CO].
 - [54] N.-M. Nguyen, F. Schmidt, B. Tucci, M. Reinecke, and A. Kostić, How much information can be extracted from galaxy clustering at the field level? (2024), arXiv:2403.03220 [astro-ph.CO].
 - [55] F. Spezzati, M. Marinucci, and M. Simonović, Equivalence of the field-level inference and conventional analyses on large scales (2025), arXiv:2507.05378 [astro-ph.CO].
 - [56] K. Akitsu, M. Simonović, S.-F. Chen, G. Cabass, and M. Zaldarriaga, Cosmology inference with perturbative forward modeling at the field level: a comparison with joint power spectrum and bispectrum analyses (2025), arXiv:2509.09673 [astro-ph.CO].
 - [57] R. Scoccimarro, Fast Estimators for Redshift-Space Clustering, *Phys. Rev. D* **92**, 083532 (2015), arXiv:1506.02729 [astro-ph.CO].
 - [58] E. Sefusatti, M. Crocce, S. Pueblas, and R. Scoccimarro, Cosmology and the Bispectrum, *Phys. Rev. D* **74**, 023522 (2006), arXiv:astro-ph/0604505.
 - [59] Y.-S. Song, A. Taruya, and A. Oka, Cosmology with anisotropic galaxy clustering from the combination of power spectrum and bispectrum, *Journal of Cosmology and Astroparticle Physics* **2015** (08), 007–007.
 - [60] N. Kaiser, On the Spatial correlations of Abell clusters, *Astrophys. J. Lett.* **284**, L9 (1984).
 - [61] J. M. Bardeen, J. R. Bond, N. Kaiser, and A. S. Szalay, The Statistics of Peaks of Gaussian Random Fields, *Astrophys. J.* **304**, 15 (1986).
 - [62] J. L. Tinker, B. E. Robertson, A. V. Kravtsov, A. Klypin, M. S. Warren, G. Yepes, and S. Gottlober, The Large Scale Bias of Dark Matter Halos: Numerical Calibration and Model Tests, *Astrophys. J.* **724**, 878 (2010), arXiv:1001.3162 [astro-ph.CO].
 - [63] T. Lazeyras and F. Schmidt, Beyond LIMD bias: a measurement of the complete set of third-order halo bias parameters, *JCAP* **09**, 008, arXiv:1712.07531 [astro-ph.CO].
 - [64] T. Lazeyras, C. Wagner, T. Baldauf, and F. Schmidt, Precision measurement of the local bias of dark matter halos, *JCAP* **02**, 018, arXiv:1511.01096 [astro-ph.CO].
 - [65] A. Eggemeier, R. Scoccimarro, R. E. Smith, M. Crocce, A. Pezzotta, and A. G. Sánchez, Testing one-loop galaxy bias: Joint analysis of power spectrum and bispectrum, *Phys. Rev. D* **103**, 123550 (2021), arXiv:2102.06902 [astro-ph.CO].
 - [66] K. Akitsu, Mapping the galaxy-halo connection to the galaxy bias: implication to the HOD-informed prior (2024), arXiv:2410.08998 [astro-ph.CO].
 - [67] M. M. Ivanov, Simulation-Based Priors without Simulations: an Analytic Perspective on EFT Parameters of Galaxies (2025), arXiv:2503.07270 [astro-ph.CO].
 - [68] R. K. Sheth, K. C. Chan, and R. Scoccimarro, Nonlocal Lagrangian bias, *Phys. Rev. D* **87**, 083002 (2013), arXiv:1207.7117 [astro-ph.CO].